atmosphere

MDPI

Article

Deciphering Air Pollution Dynamics and Drivers in Riverine Megacities Using Remote Sensing Coupled with Geospatial Analytics for Sustainable Development

Almustafa Abd Elkader Ayek [1], Mohannad Ali Loho [2,3], Wafa Saleh Alkhuraiji [4], Safieh Eid [2], Mahmoud E. Abd-Elmaboud [5], Faten Nahas [6] and Youssef M. Youssef [7,*]

1 Department of Topography, Faculty of Civil Engineering, University of Aleppo, Aleppo P.O. Box 12212, Syria
2 Department of Geography, Faculty of Arts and Humanities, Damascus University, Damascus P.O. Box 30621, Syria
3 Department of Geography, Faculty of Arts and Humanities, Tartous University, Tartous P.O. Box 2147, Syria
4 Department of Geography and Environmental Sustainability, College of Humanities and Social Sciences, Princess Nourah bint Abdulrahman University, P.O. Box 84428, Riyadh 11671, Saudi Arabia
5 Irrigation & Hydraulics Department, Faculty of Engineering, Mansoura University, Mansoura 35516, Egypt
6 Department of Geography, College of Humanities and Social Sciences, King Saud University, Riyadh 11451, Saudi Arabia
7 Geological and Geophysical Engineering Department, Faculty of Petroleum and Mining Engineering, Suez University, Suez 43518, Egypt
* Correspondence: youssef.ibrahim@pme.suezuni.edu.eg

Abstract

Air pollution represents a critical environmental challenge in stressed riverine cities, particularly in regions experiencing rapid urbanization and inadequate emission management infrastructure. This study investigates the spatio-temporal dynamics of atmospheric pollution in Baghdad, Iraq, during 2012–2023, analyzing seven key pollutants (CO, CO_2, SO_2, SO_4, O_3, CH_4, and AOD) using NASA's Giovanni platform coupled with Google Earth Engine analytics. Monthly time-series data were processed through advanced statistical techniques, including Seasonal Autoregressive Integrated Moving Average (SARIMA) modeling and correlation analysis with meteorological parameters, to identify temporal trends, seasonal variations, and driving mechanisms. The analysis revealed three distinct pollutant trajectory categories reflecting complex emission–atmosphere interactions. Carbon monoxide exhibited dramatic decline (60–70% reduction from 2021), attributed to COVID-19 pandemic restrictions and demonstrating rapid responsiveness to activity modifications. Conversely, greenhouse gases showed persistent accumulation, with CO_2 increasing from 400.5 to 417.5 ppm and CH_4 rising 5.9% over the study period, indicating insufficient mitigation efforts. Sulfur compounds and ozone displayed stable concentrations with pronounced seasonal oscillations (winter peaks 2–3 times summer levels), while aerosol optical depth showed high temporal variability linked to dust storm events. Spatial analysis identified pronounced urban–rural concentration gradients, with central Baghdad CO levels exceeding 0.40 ppm compared to peripheral regions below 0.20 ppm. Linear concentration patterns along transportation corridors and industrial zones confirmed anthropogenic source dominance. Correlation analysis revealed strong relationships between meteorological factors and pollutant concentrations (atmospheric pressure: r = 0.62–0.70 with NO_2), providing insights for integrated climate–air quality management strategies. The study demonstrates substantial contributions to Sustainable Development Goals across four dimensions (Environmental Health 30%, Sustainable Cities and Climate Action 25%, Economic Development 25%, and Institutional Development 20%) while providing transferable methodological frameworks for evidence-based policy interventions and environmental monitoring in similar stressed urban environments globally.

check for updates

Academic Editors: Mei Li, Enrico Ferrero, Mingyue Lu, Hua Shao and Hui Liu

Received: 28 July 2025
Revised: 26 August 2025
Accepted: 9 September 2025
Published: 15 September 2025

Citation: Ayek, A.A.E.; Loho, M.A.; Alkhuraiji, W.S.; Eid, S.; Abd-Elmaboud, M.E.; Nahas, F.; M. Youssef, Y. Deciphering Air Pollution Dynamics and Drivers in Riverine Megacities Using Remote Sensing Coupled with Geospatial Analytics for Sustainable Development. *Atmosphere* **2025**, *16*, 1084. https://doi.org/10.3390/atmos16091084

Copyright: © 2025 by the authors. Licensee MDPI, Basel, Switzerland. This article is an open access article distributed under the terms and conditions of the Creative Commons Attribution (CC BY) license (https://creativecommons.org/licenses/by/4.0/).

Keywords: air pollution dynamics; remote sensing; google earth engine; Baghdad; spatio-temporal analysis; sustainable development goals; stressed riverine cities

1. Introduction

Air pollution is a critical challenge affecting urban regions worldwide, inflicting substantial impacts not only on public health and environmental sustainability but also on economic productivity and social equity [1–4]. In developing countries, these adverse effects are particularly pronounced due to rapid demographic growth, geographic vulnerabilities, and limited regulatory and infrastructural capacities [5]. Baghdad, as Iraq's capital and most populous metropolis, exemplifies an urban area where unchecked urbanization, intensive industrialization, and persistent underinvestment in environmental systems have driven pollution to levels hazardous to both human populations and the environment [6–8].

Unlike many global megacities where transboundary pollution or natural phenomena dominate, Baghdad's air quality crisis is rooted overwhelmingly in local anthropogenic sources. Over 90% of hazardous fine particulate matter in the city arises from diesel generators, chronic traffic congestion, and unregulated industrial emissions, contradicting earlier attributions to regional dust storms [9,10]. Infrastructural deterioration, exacerbated by decades of conflict and sanctions, has fostered heavy reliance on high-emission energy sources, particularly where electricity grids are unreliable [6,9]. The situation is further aggravated by frequent dust storms, extreme heat events, and meteorological phenomena such as summer inversions and dry winds, all of which contribute to pollutant accumulation and secondary chemical transformation [11].

Recent assessments indicate that annual mean $PM_{2.5}$ concentrations in Baghdad exceed 70 $\mu g/m^3$—more than 14 times the WHO guideline limit of 5 $\mu g/m^3$—while NO_2 and SO_2 levels frequently surpass international standards during both summer and winter seasons [12–14]. In comparison with other Middle Eastern cities, Baghdad shares regional characteristics such as frequent dust intrusions, arid climatic conditions, and seasonal photochemical smog events. However, it is distinguished by a higher contribution of local anthropogenic sources, limited air quality monitoring infrastructure, and socio-economic constraints that hinder effective mitigation [15–17].

The atmospheric environment over urban areas in the Middle East faces unprecedented challenges from multiple pollutant categories that collectively threaten both human health and environmental sustainability. This study investigates seven critical atmospheric pollutants that represent diverse emission sources, chemical processes, and environmental impacts in the Baghdad metropolitan region. Carbon monoxide represents one of the most critical atmospheric pollutants due to its silent but deadly characteristics, functioning as a colorless, odorless gas produced primarily through incomplete combustion processes that poses significant health risks by binding to hemoglobin with an affinity approximately 200 times greater than oxygen, severely compromising cellular oxygen transport and potentially leading to fatal poisoning [18,19]. Carbon dioxide represents the most significant anthropogenic greenhouse gas, fundamentally altering Earth's radiative balance and driving contemporary climate change through its dramatic elevation since the Industrial Revolution due to fossil fuel combustion, deforestation, and industrial activities, with atmospheric residence times of centuries making it a cumulative indicator of global carbon cycle perturbations [20,21]. Sulfur dioxide represents a critical atmospheric pollutant originating primarily from fossil fuel combustion in power plants and industrial processes, exhibiting relatively short atmospheric residence times that make regional concentrations highly sensitive to local emission sources and meteorological con-

ditions [22]. Atmospheric sulfates constitute a critical component of secondary particulate matter formation, with anthropogenic activities becoming the dominant source through sulfur dioxide oxidation reactions—including OH-driven oxidation under Baghdad's hot, sunny, and dry climate—creating sulfate-containing fine particulate matter directly linked to increased cardiovascular and respiratory mortality rates [23,24]. Tropospheric ozone in such environments is often produced via photochemical reactions involving NO_x, CO, VOCs, and radicals such as OH, and its correlation with SO_4 is largely driven by shared oxidation chemistry rather than direct causality [25,26]. Methane functions as the second most impactful greenhouse gas contributing to global warming after carbon dioxide, originating from wetlands through anaerobic microbial activity, agricultural sources particularly rice cultivation, and fossil fuel extraction, accounting for approximately 25% of greenhouse gas-induced warming despite its relatively short atmospheric lifespan of 10–12 years [27–29]. Aerosol Optical Depth measures the extent of light absorption and scattering by atmospheric particles, reflecting fine particulate matter concentrations that penetrate respiratory systems causing asthma and chronic lung diseases while exerting significant radiative forcing effects that influence regional and global climate patterns through cooling effects from sulfur aerosols or warming from black carbon particles [30,31].

The consequences of this air pollution extend far beyond environmental degradation. Healthcare costs associated with pollution, coupled with lost labor productivity and crop damages, absorb a significant proportion of national resources in low- and middle-income states. According to the World Bank, According to Heger et al. (2022), air pollution-related health damages in the Middle East and North Africa cost around $141 billion per year, or 2% of regional GDP, with Iraq specifically experiencing welfare losses of 2.67% of GDP annually [32,33].

Additional compounding factors include land-use change and the intensification of the urban heat island effect [34], which enhances photochemical reactions and modifies local wind and precipitation patterns, creating an environment conducive to secondary pollutant formation, such as ozone and sulfates [6,35]. Such processes highlight the tight coupling between air quality and climate; accumulations of fine particulates and greenhouse gases significantly modify local atmospheric conditions, with emerging implications for precipitation patterns, drought, and water security [10,35].

Monitoring these complex urban atmospheric dynamics has historically been difficult in Iraq and the broader Middle East, largely due to chronic underinvestment in environmental infrastructure. Regional instability, population displacements, and substantial gaps in ground-based sensor networks have left major cities without continuous, reliable air quality data [36,37]. Advanced satellite remote sensing technologies thus became an essential means to bridge this data gap. However, until the launch of Sentinel-5P TROPOMI in October 2017 (operational from mid-2018), long-term consistent satellite observations for certain gases were not available, which led this study to rely primarily on MERRA-2 reanalysis products, subsequently enhanced using cubic convolution interpolation to improve spatial resolution. [22,36,38]. Recent deployments, such as TROPOMI and the multi-sensor NASA Giovanni platform, now enable urban air quality assessments at scales capable of detecting neighborhood and source-level patterns [37,39]. Alternative platforms such as Google Earth Engine (GEE) and Copernicus Atmosphere Monitoring Service (CAMS) could be applied; however, Giovanni was selected due to its balance between accessibility, dataset integration, and compatibility with the study's temporal scope.

Methodological breakthroughs, particularly those catalyzed by the COVID-19 pandemic, have elevated the accuracy, relevance, and applicability of satellite-based air quality research. Sophisticated statistical models such as the Seasonal Autoregressive Integrated Moving Average (SARIMA) model [40], combined with machine learning techniques, now

allow researchers to disentangle the effects of emissions, meteorology, and policy interventions on atmospheric pollutant trends, enabling more robust forecasting for public health and environmental management [41,42]. Such approaches are particularly apt for assessing both routine and extraordinary events, including pandemic lockdowns or severe droughts, thereby providing actionable evidence for policymakers [43].

Baghdad's atmospheric composition is notably diverse, featuring elevated concentrations of carbon monoxide (CO), carbon dioxide (CO_2), sulfur dioxide (SO_2), sulfates (SO_4), ozone (O_3), methane (CH_4), and fine particulates indexed by aerosol optical depth (AOD). Each pollutant has distinct sources, transformation pathways, and health impacts, ranging from acute respiratory and cardiovascular conditions to long-term alterations in the urban climate [10,23,24]. The combined presence and complex interaction of these compounds under Iraq's extreme meteorological regimes create a challenging, dynamic, and variable atmospheric environment.

Despite substantial progress in satellite remote sensing and analytics, significant research and policy gaps persist in air quality management for Baghdad and the broader region. The chronic lack of dense ground-based monitoring and calibration networks hampers the validation and contextualization of satellite data [7,37], complicating accurate assessments of source-receptor dynamics, atmospheric transport, and the efficacy of emission mitigation strategies. These deficits are compounded by the complex interaction of meteorological, emission, and natural factors characterizing Baghdad's urban environment. Furthermore, most previous studies suffer from limited duration, narrow pollutant focus, or insufficient spatial detail, leaving critical processes such as secondary pollutant formation, greenhouse gas accumulation, and the impacts of episodic events like the COVID-19 lockdown only partially understood [6,10,41,44]. Chronic underinvestment in environmental research and technology, further exacerbated by periods of political instability, has delayed the adoption of systematic, transparent, and reproducible air quality monitoring, undermining Iraq's commitments to Sustainable Development Goals (SDG 3.9.1, 11.6.2), which call for measurable improvements and reliable, openly accessible environmental data [33,45,46]. The resulting deficit in robust, long-term, and high-resolution data not only limits the effectiveness of evidence-based policy in Iraq but also impedes regional and international collaboration in urban air pollution management, a gap directly targeted by the present study.

This research directly addresses these gaps in air quality monitoring and analysis for Baghdad Governorate by leveraging NASA's Geospatial Interactive Online Visualization and analysis Infrastructure (Giovanni) platform to execute a comprehensive decadal (2012–2023) time-series investigation of seven primary atmospheric pollutants: carbon monoxide (CO), carbon dioxide (CO_2), sulfur dioxide (SO_2), sulfates (SO_4), ozone (O_3), methane (CH_4), and aerosol optical depth (AOD). Employing advanced statistical, geospatial, and machine learning methodologies, the study systematically examines the temporal and seasonal dynamics of these pollutants. Specifically, it seeks to (1) elucidate the principal drivers and spatiotemporal patterns of Baghdad's recurrent air quality challenges; (2) quantify the specific impacts of anthropogenic activities and episodic disturbances, including the COVID-19 lockdown, on pollutant behaviors; and (3) formulate evidence-based recommendations for integrated and sustainable air quality management. Through the production of robust baseline data and decadal analytical insights, this study advances both scientific understanding and practical policy action for managing urban air pollution in a region where comprehensive monitoring and environmental investments remain limited.

2. Materials and Methods

2.1. Study Area

Baghdad Governorate, the capital and largest metropolitan area of Iraq, is strategically positioned in the central region of Mesopotamia between latitudes 33°02′ to 33°58′ N and longitudes 44°08′ to 44°58′ E (Figure 1). The governorate encompasses an area of approximately 4555 square kilometers, with the urban core spanning 673 square kilometers along the banks of the Tigris River, one of the region's most significant waterways [6]. This location places Baghdad within the fertile alluvial plains of ancient Mesopotamia, which have historically been recognized as among the most agriculturally productive regions in the Middle East due to their rich sedimentary deposits and favorable hydrological conditions.

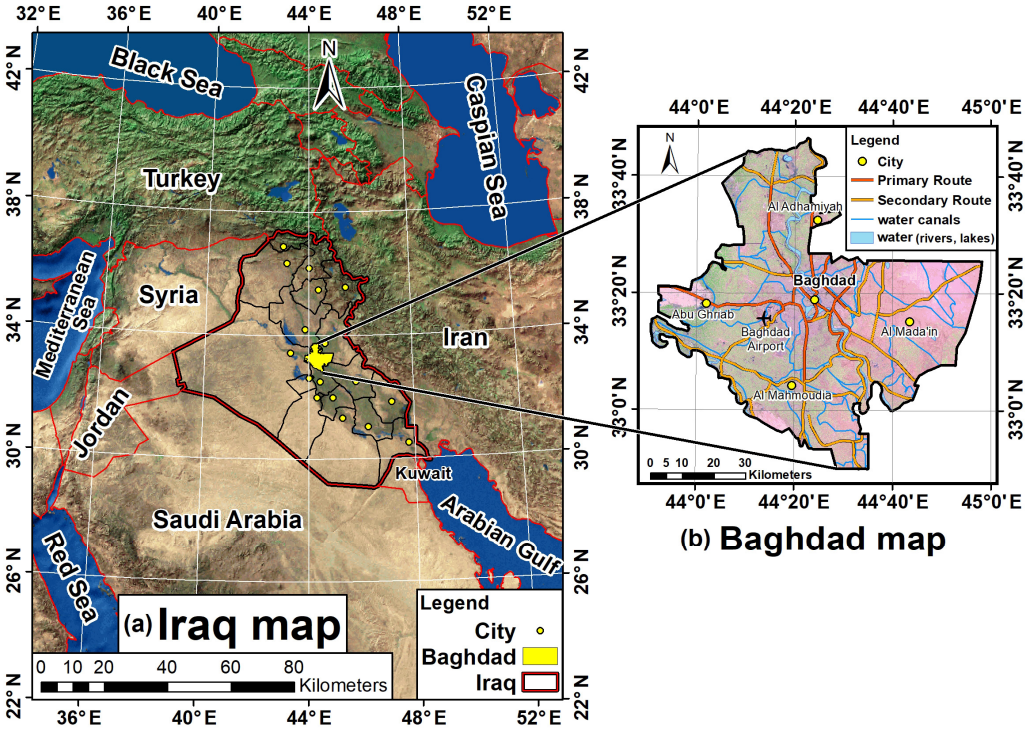

Figure 1. Geographic location of Baghdad Governorate within Iraq: (**a**) Location of Iraq in the Middle East region, (**b**) Administrative boundaries of Baghdad Governorate showing its position along the Tigris River in central Iraq.

The city's geographical setting has profound implications for air quality dynamics. Baghdad lies at an elevation ranging from 31 to 40 m above sea level, creating a relatively flat topography that can facilitate pollutant accumulation under certain meteorological conditions [9]. The surrounding landscape is characterized by expansive plains extending in all directions, with minimal topographical barriers that could influence wind patterns or atmospheric dispersion of pollutants. In addition, Baghdad's semi-arid continental climate, characterized by extremely hot summers (often exceeding 45 °C) and mild winters with low annual precipitation (<150 mm) [47], enhances photochemical activity and accelerates secondary pollutant formation such as ozone and sulfates under high solar radiation conditions [48].

Baghdad has experienced remarkable demographic transformation over recent decades, with population growth from approximately 3.8 million inhabitants in the 1980s to over 8.8 million currently, representing one of the highest population densities in the Middle East region [7]. This equates to an average density exceeding 1930 inhabitants/km^2 in the urbanized core, a figure significantly above the national average. This rapid urbanization has been accompanied by extensive land-use modifications that have fundamentally

altered the environmental characteristics of the area. Historical agricultural lands that once dominated the urban periphery have been systematically converted into residential developments, commercial districts, and industrial complexes, significantly reducing the natural vegetation cover that previously contributed to local air purification processes [49].

The urban morphology of Baghdad reflects typical patterns of unplanned metropolitan expansion in developing regions, with concentrated development along the Tigris River corridor creating high-density urban centers. These riverside areas have become focal points for economic activities, governmental institutions, and commercial enterprises, resulting in increased vehicular traffic, energy consumption, and associated emissions [10]. The concentration of anthropogenic activities in these areas, coupled with the city's role as Iraq's primary administrative and economic hub, has established Baghdad as a significant source of various atmospheric pollutants that are the focus of this study.

The governorate's position within Iraq's broader geographical context also influences its air quality dynamics through regional pollutant transport mechanisms. Baghdad receives atmospheric inputs from both local sources and distant regions, including dust storms originating from western desert areas and transboundary pollution from neighboring countries [11]. These interactions between local and regional sources highlight the necessity of integrating satellite-based remote sensing with ground-based measurements, as the latter often have sparse coverage and cannot capture the full extent of long-range transport phenomena [7].

2.2. Methodological Framework

This study employs a comprehensive satellite remote sensing approach to monitor atmospheric pollutant trends across Baghdad Governorate during the period from 2012 to 2023. The methodology integrates advanced data acquisition from NASA's Giovanni platform with sophisticated Python-based analytical tools to provide comprehensive temporal and spatial assessment of air quality patterns. Recent developments in satellite remote sensing have demonstrated enhanced capabilities for atmospheric monitoring, with modern Earth observation systems providing measurements of finer spatial, temporal, and radiometric resolution with increased global coverage. The analytical framework is designed to address the critical need for robust air quality monitoring in regions where ground-based infrastructure is limited, particularly in the context of sustainable development goals related to environmental health.

While most datasets are derived from MERRA-2 reanalysis products—which integrate satellite observations with atmospheric models via data assimilation techniques [50]—the study also addresses their relatively coarse native resolution by applying cubic convolution resampling to achieve ~0.01° spatial detail. This enhancement approach, widely used in geospatial research [51,52], helps capture finer-scale variability in urban areas where in situ observations are sparse, while preserving the statistical integrity of the original data.

The research methodology follows a systematic three-phase approach that encompasses data acquisition and preprocessing, spatial enhancement through advanced interpolation techniques, and comprehensive temporal analysis. This integrated approach enables the characterization of complex atmospheric pollution patterns while maintaining scientific rigor and reproducibility. Satellite remote sensing has proven particularly valuable for real-time monitoring of emission regimes, with daily global-scale remote sensing data providing exceptional insights into atmospheric pollutant distributions.

2.2.1. Data Sources and Platform Selection

This investigation utilized atmospheric pollutant concentration data obtained through advanced satellite-based remote sensing measurements. The data acquisition relies on sophisticated spectrometers operating across infrared, visible, and ultraviolet spectral ranges aboard Earth observation satellites, which detect spectral variations caused by atmospheric absorption and scattering processes as solar and terrestrial radiation passes through the atmosphere. These spectral signatures are subsequently processed using retrieval algorithms incorporating radiative transfer models to generate quantitative estimates of atmospheric gas concentrations, with regular validation against ground-based measurements ensuring data accuracy and reliability [53].

Monthly atmospheric pollutant data were systematically extracted from NASA's Giovanni platform for seven key atmospheric indicators: total column ozone (O_3), aerosol optical depth (AOD), methane (CH_4), surface carbon monoxide (CO), dry air column-averaged carbon dioxide (CO_2), sulfur dioxide (SO_2), and sulfate (SO_4) column mass density. Giovanni serves as a comprehensive web-based data analysis and visualization system that provides access to multiple satellite-derived atmospheric composition products with global coverage and consistent temporal resolution. The platform facilitates the extraction and preliminary analysis of air quality data across varying spatial and temporal scales, making it particularly suitable for regional atmospheric monitoring studies [54].

Notably, Sentinel-5P TROPOMI products—initially delivered at a spatial resolution of approximately 7 × 3.5 km at nadir—were later improved after 2019 to reach ~1 km resolution for several species. However, these higher-resolution datasets cover only a subset of pollutants, and do not include all the atmospheric constituents analyzed in this study (SO_4, and AOD). Therefore, while Sentinel-5P data could enrich recent comparative mapping, their limited temporal coverage (from late 2017 onward) and incomplete pollutant representation prevented their use for the consistent decadal (2012–2023) trend analysis undertaken [51,52].

The selected datasets encompassed seven key atmospheric pollutants and indicators as detailed in Table 1, which provides comprehensive specifications for each data product including source models, spatial and temporal resolutions, and temporal coverage periods. The majority of datasets utilized MERRA-2 (Modern-Era Retrospective analysis for Research and Applications, Version 2) reanalysis products, providing consistent spatial resolution of 0.5° × 0.625° with monthly temporal resolution. Additional datasets included AIRS (Atmospheric Infrared Sounder) retrievals with 1° spatial resolution for methane observations, and GEOS-CHEM model outputs for CO_2 analysis, ensuring comprehensive coverage of key atmospheric constituents.

These seven indicators (CO, CO_2, SO_2, SO_4, O_3, CH_4, and AOD) were specifically selected because they represent the major categories of air quality drivers: primary combustion pollutants (CO, SO_2), greenhouse gases (CO_2, CH_4), secondary aerosol formation (SO_4^{2-}), atmospheric oxidants (O_3), and total aerosol loading (AOD). Together, they provide a sufficiently representative set to capture both health-related and climate-relevant aspects of urban air quality, while being consistently available in long-term global reanalysis datasets [3,55].

The temporal scope of this analysis spans from 2012 to 2023, utilizing monthly composite data products to ensure comprehensive seasonal and interannual variability assessment. Spatial resolution varied among products, ranging from 0.5° × 0.625° for MERRA-2 reanalysis products to 1° for AIRS retrievals, providing adequate detail for governorate-level analysis while maintaining data consistency across different satellite platforms. All datasets were resampled to a uniform 0.01° resolution using cubic convolution interpolation, a technique shown to improve visualization and spatial comparability of

coarse-resolution climate and atmospheric datasets [51,52]. Data extraction and processing were conducted using Python (version 3.10.12) programming on the Google Colab platform (https://colab.research.google.com/, accessed on 22 March 2025), employing cubic resampling techniques to maintain spatial accuracy during map generation. Temporal and spatial visualization of pollutant distributions was achieved through specialized plotting libraries, enabling comprehensive assessment of long-term trends and seasonal patterns across Baghdad Governorate. The platform's capability to handle large volumes of heterogeneous satellite data from multiple sources makes it particularly suitable for long-term atmospheric monitoring studies, providing an unprecedented 12-year continuous dataset for comprehensive trend analysis.

Table 1. Atmospheric Pollutant Datasets Retrieved from NASA Giovanni Platform.

Atmospheric Indicator	Product Name (Version)	Units	Source/ Model	Data Resolution		Temporal Coverage	
				Temporal	Spatial	Start Date	End Date
Total Column Ozone (O_3)	M2TMNXCHM v5.12.4	Dobsons	MERRA-2 Reanalysis	Monthly	0.5° × 0.625°	1 January 1980	30 June 2025
Aerosol Optical Depth (AOD)	M2IMNXGAS v5.12.4	-	MERRA-2 Reanalysis	Monthly	0.5° × 0.625°	1 January 1980	30 June 2025
Methane Mole Fraction (CH_4)	AIRS3STM v006	ppbv	AIRS	Monthly	1°	1 September 2002	30 June 2025
Surface Carbon Monoxide (CO)	M2TMNXCHM v5.12.4	ppbv	MERRA-2 Reanalysis	Monthly	0.5° × 0.625°	1 January 1980	30 June 2025
Dry Air Column-Averaged CO_2	OCO2_GEOS_L3CO 2_MONTH v10r	ppm	data	Monthly	0.5° × 0.625°	1 January 2015	28 February 2022
Sulfur Dioxide Column Mass Density (SO_2)	M2TMNXAER v5.12.4	kg/m^2	MERRA-2 Reanalysis	Monthly	0.5° × 0.625°	1 January 1980	30 June 2025
Sulfate Column Mass Density (SO_4)	M2TMNXAER v5.12.4	kg/m^2	MERRA-2 Reanalysis	Monthly	0.5° × 0.625°	1 January 1980	30 June 2025

Note: All datasets were accessed through NASA's Giovanni platform (https://giovanni.gsfc.nasa.gov/giovanni/ accessed on 20 March 2025). MERRA-2: Modern-Era Retrospective analysis for Research and Applications, Version 2; AIRS: Atmospheric Infrared Sounder; GEOS-CHEM: Goddard Earth Observing System-Chemistry model; ppbv: parts per billion by volume; ppm: parts per million.

2.2.2. Quality Control and Data Preparation

Rigorous quality control procedures were implemented to ensure data integrity and reliability throughout the analysis. These procedures included systematic identification and removal of data gaps, comprehensive cloud contamination screening, and temporal consistency verification across the eleven-year study period. Monthly composite datasets were generated to minimize the influence of short-term atmospheric variations and provide robust seasonal pattern analysis suitable for long-term trend detection.

The monthly average concentration for each atmospheric pollutant was calculated using the following fundamental equation [56]:

$$C_{avg}^{(m)}(x,y) = \frac{1}{N_m} \sum_{t \in T_m} C_t(x,y) \quad (1)$$

where $C_{avg}^{(m)}(x,y)$ represents the monthly average gas concentration for month m at coordinates (x,y); T_m denotes the set of dates containing data for month m; Nm is the number of valid observations for month m, and $C_t(x,y)$ is the pollutant concentration at time t and location (x,y).

This averaging approach effectively reduces temporal noise while preserving meaningful seasonal and annual variations essential for trend analysis.

2.2.3. Spatial Enhancement and Mapping

To enhance spatial accuracy and ensure consistent representation across different satellite products, cubic resampling was employed following the Keys (1981) interpolation method [57]. This method was chosen over bilinear or nearest-neighbor interpolation because it preserves gradient continuity while avoiding excessive smoothing, which is essential for detecting subtle pollutant concentration differences in urban areas [57,58]. Advanced spatial interpolation techniques have been recognized as essential for atmospheric monitoring applications, particularly when dealing with irregularly distributed satellite observations. This method provides smooth spatial interpolation while preserving original data characteristics and maintaining the integrity of concentration gradients across the study region. The cubic interpolation process follows the Keys formula, which aggregates information from 16 neighboring pixels within a computational matrix:

$$f(x,y) = \sum_{i=-1}^{2} \sum_{j=-1}^{2} h(i-x) \cdot h(j-y) \cdot f(i,j) \quad (2)$$

The interpolation weight function $h(s)$ is calculated using the cubic Keys function:

$$h(s) = \begin{cases} 1.5|s|^3 - 2.5|s|^2 + 1, & 0 \leq |s| < 1 \\ -0.5|s|^3 + 2.5|s|^2 - 4|s| + 2, & 1 \leq |s| < 2 \\ 0, & |s| \geq 2 \end{cases} \quad (3)$$

where s represents the normalized distance from the interpolation point to the data point. This cubic interpolation approach ensures smooth transitions between data points while maintaining local gradient information critical for accurate pollutant concentration mapping.

All mapping and visualization procedures were implemented using Python programming language within the Google Colab cloud computing environment. This setup ensured both reproducibility and accessibility, as all code, dependencies, and runtime environments can be shared via Colab notebooks without platform-specific constraints [59]. The computational framework leveraged several specialized libraries optimized for geospatial analysis and atmospheric data processing. The core libraries utilized included numpy v1.23.5 for numerical computations, scipy v1.10.1 for cubic interpolation operations, rasterio v1.3.8 for GeoTIFF data handling, and matplotlib v3.7.1 combined with cartopy v0.21.1 for generating high-quality geographical visualizations.

This cloud-based computational environment facilitated efficient processing of large satellite datasets while enabling the generation of publication-quality geographical visualizations optimized for atmospheric pollutant data representation. The standardized computational environment ensures reproducibility of results and enables efficient scaling for extended temporal or spatial analyses.

2.2.4. Temporal Analysis and Trend Assessment

Comprehensive time series analysis focused on identifying long-term trends and seasonal patterns through specialized temporal analytical approaches. Prior to analysis, all pollutant concentrations were converted to standard units (ppm or ppbv as appropriate) using molecular weight adjustments where necessary to ensure inter-pollutant comparability. The temporal analysis framework encompasses three complementary analytical dimensions: monthly variations for seasonal cycle characterization, annual trends for long-term change assessment, and overall patterns for comprehensive environmental shift evaluation. The monthly average concentration for each atmospheric pollutant over Baghdad city was calculated by spatially aggregating pixel values within the city boundaries:

$$\bar{C}_m^{(y)} = \frac{1}{n} \sum_{(x,y)\in \mathrm{B}} C_m^{(y)}(x,y) \tag{4}$$

where $\bar{C}_m^{(y)}$ represents the spatially averaged concentration for month m of year y; B denotes the set of pixels located within Baghdad city boundaries; n is the total number of pixels within Baghdad's administrative boundaries, and $C_m^{(y)}(x,y)$ is the pollutant concentration at location (x,y) for month m of year y.

Two complementary time series were constructed:

General monthly series covering the full study period:

$$\mathrm{TS} = \left\{\bar{C}_1, \bar{C}_2, ..., \bar{C}_T\right\} \tag{5}$$

Month-specific seasonal series:

$$\mathrm{TS}_m = \left\{\bar{C}_m^{(y_1)}, \bar{C}_m^{(y_2)}, \ldots, \bar{C}_m^{(y_N)}\right\} \tag{6}$$

Long-term trend evaluation was conducted using ordinary least squares (OLS) regression with heteroskedasticity-robust standard errors [60]:

$$\hat{C}_t = \beta_0 + \beta_1 t + \epsilon_t \tag{7}$$

where β_1 de provides the rate of change per unit time. Statistical significance was evaluated using two-tailed t-tests at the 95% confidence level.

Visualization products were created using numpy v1.23.5, pandas v1.5.3, statsmodels v0.13.5, scipy.stats v1.10.1, matplotlib v3.7.1, and seaborn v0.12.2. Color palettes were adapted from ColorBrewer schemes to ensure perceptual uniformity and accessibility for color-impaired viewers [61,62]. The analytical framework illustrated in Figure 2 demonstrates the streamlined approach adopted for this satellite-based air quality assessment—from data acquisition and quality control to cubic resampling, temporal analysis, and mapping—providing a reproducible workflow suitable for replication in other urban environments with limited in situ monitoring and for informing both scientific research and policy making.

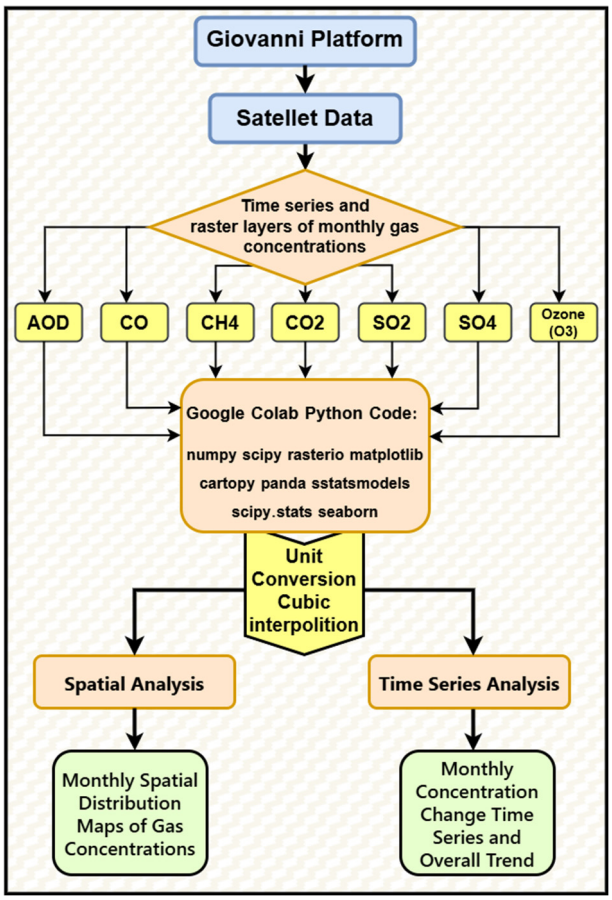

Figure 2. Methodology for Data Acquisition and Processing.

3. Results and Discussion

3.1. Temporal Trends and Long-Term Variations of Atmospheric Pollutants (2012–2023)

The comprehensive analysis of seven critical atmospheric pollutants over Baghdad from 2012 to 2023 reveals distinct temporal patterns that reflect the complex interplay between emission sources, atmospheric processes, and external forcing factors. Figure 3 presents the long-term trend analysis for all studied pollutants, while detailed monthly variations are provided in the Supplementary Material (Figures S1–S7), demonstrating three primary trajectory categories: declining, stable with fluctuations, and increasing trends that provide crucial insights into regional air quality dynamics and emission management effectiveness.

Carbon monoxide exhibits the most dramatic temporal transformation among all studied pollutants, characterized by two distinct phases that fundamentally altered the atmospheric CO landscape (Figure 3a). During the initial phase (2012–2020), CO concentrations maintained relatively stable levels around 0.35–0.40 ppm with characteristic seasonal oscillations ranging from winter peaks of 0.45–0.50 ppm to summer minima of 0.25 ppm (Supplementary Figure S1). However, beginning in 2021, a precipitous decline occurred, with concentrations dropping by 60–70% to baseline levels of 0.10–0.15 ppm. Statistical analysis reveals a biphasic trend with $R^2 = 0.78$ ($p < 0.001$) for the overall period, where R^2 (coefficient of determination) indicates the proportion of variance explained by the trend line and p-value represents the statistical significance probability, while the standard deviation decreased from 0.08 ppm during 2012–2020 to 0.02 ppm during 2021–2023, indicating not only reduced concentrations but also enhanced stability. This unprecedented reduction corresponds temporally with global COVID-19 pandemic restrictions, which resulted in significant decreases in transportation activities and industrial operations.

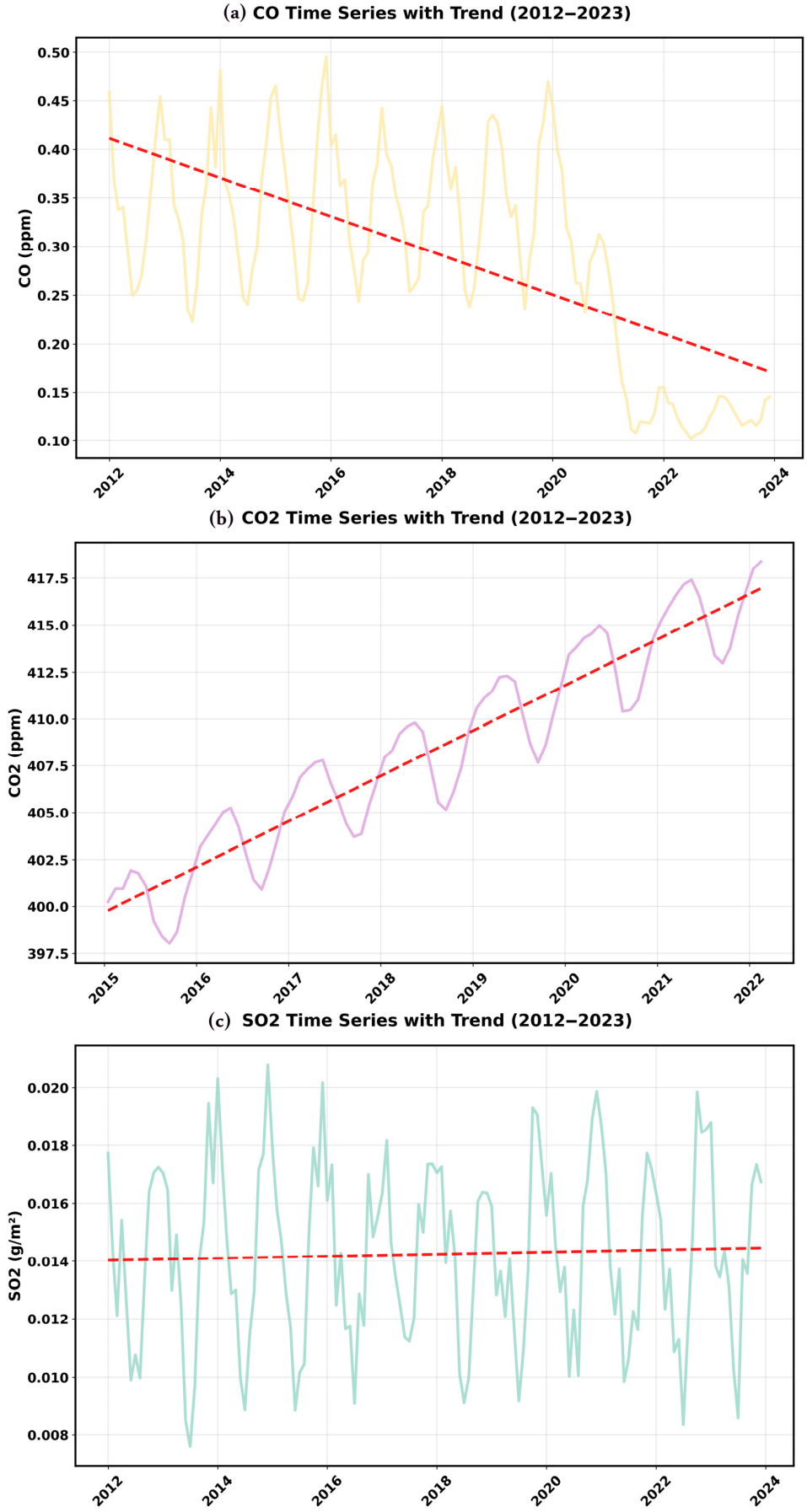

Figure 3. *Cont.*

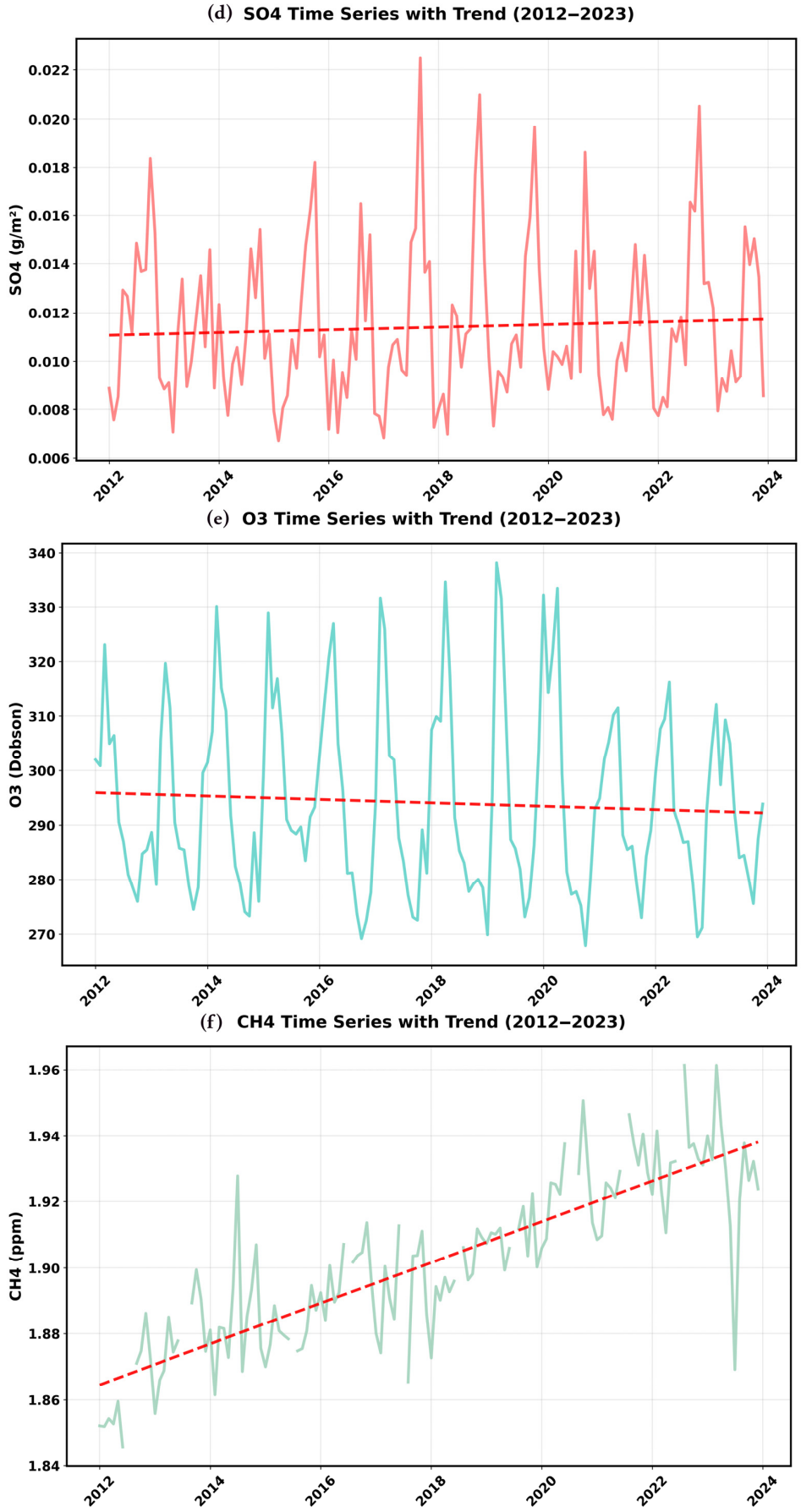

Figure 3. *Cont.*

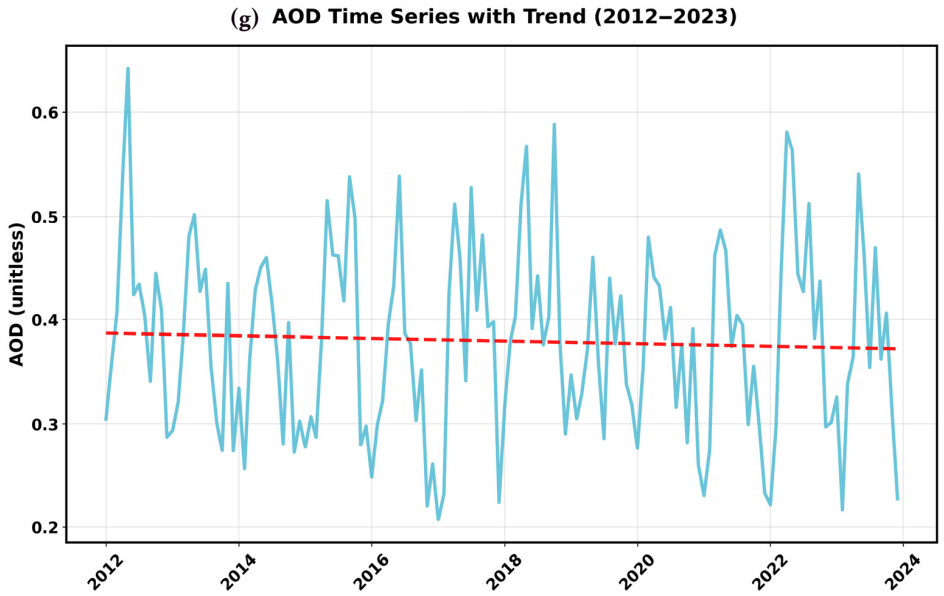

Figure 3. Illustrates the long-term trend analysis of seven key atmospheric pollutants in Baghdad Governorate for the period 2012–2023: (**a**) CO, (**b**) CO_2, (**c**) SO_2, (**d**) SO_4, (**e**) O_3, (**f**) CH_4, and (**g**) AOD concentrations. The time series of monthly mean CH_4 concentrations over Baghdad during 2012–2023 is also presented. The red dashed line represents the long-term linear trend, while data gaps (break points) correspond to intervals when original satellite observations were unavailable in the Giovanni platform.

Carbon dioxide demonstrates the most consistent increasing trend among all pollutants (Figure 3b), with concentrations showing a steady linear increase from baseline values of 400.5 ppm in 2015 to 417.5 ppm by 2022, representing a cumulative rise of 17 ppm. Statistical analysis reveals an exceptionally strong linear correlation ($R^2 = 0.98$, $p < 0.001$) with an average annual growth rate of 2.125 ppm/year and standard deviation of $\pm$1.2 ppm across the study period. Monthly analysis (Supplementary Figure S2) reveals seasonal amplitude increasing from 3.2 ppm in 2015 to 4.1 ppm in 2022, with coefficient of variation remaining consistently low at 0.3%, indicating enhanced seasonal variability alongside the overall upward trend while maintaining high temporal stability.

Methane exhibits a similar but more variable increasing pattern (Figure 3f), with concentrations rising from 1.847 ppm in 2012 to 1.956 ppm by 2023, representing a 5.9% increase over the study period (Supplementary Figure S6). Statistical analysis shows a strong positive trend ($R^2 = 0.85$, $p < 0.001$) with an average growth rate of 9.1 ppb/year and standard deviation of $\pm$0.022 ppm. Notable acceleration occurred during 2018–2022 (12–15 ppb/year) compared to 2012–2017 (6–8 ppb/year), with coefficient of variation values ranging from 1.2% in winter to 2.1% in summer, reflecting the temperature sensitivity of biogenic methane emissions.

Sulfur dioxide demonstrates relative temporal stability with high seasonal oscillations (Figure 3c), maintaining concentrations around a mean baseline of 1.25×10^{-5} kg/m^2 throughout the study period. Statistical analysis reveals no significant long-term trend ($R^2 = 0.02$, $p > 0.05$) but high seasonal variability with standard deviation of $\pm 0.35 \times 10^{-5}$ kg/m^2 and coefficient of variation of 35–40%. Seasonal amplitudes consistently show 125% variation between winter maxima (1.8–2.1 $\times 10^{-5}$ kg/m^2) and summer minima (0.75–0.8 $\times 10^{-5}$ kg/m^2) as detailed in Supplementary Figure S3, with interannual variability remaining within $\pm$5–8% of the long-term mean.

From an atmospheric chemistry perspective, the stable SO_2 levels but increasing SO_4^{2-} (Figure 3d) indicate that oxidation processes—especially the OH-initiated gas-phase pathway—are likely dominant during Baghdad's hot, sunny, semi-arid conditions [63,64]:

$$OH + SO_2 + M \rightarrow HOSO_2 + M \quad (8)$$

$$HOSO_2 + O_2 \rightarrow HO_2 + SO_3 \quad (9)$$

$$SO_3 + H_2O \rightarrow H_2SO_4(g/cond.) \quad (10)$$

In humid or high-pH aerosol conditions, aqueous-phase reactions with H_2O_2 and O_3 can become significant [65–67]:

$$HSO_3^- + H_2O_2 \rightarrow HSO_4^- + H_2O \quad (11)$$

$$HSO_3^- + O_3 \rightarrow HSO_4^- + O_2 \quad (12)$$

NO_2/HONO multiphase pathways and heterogeneous metal-catalyzed reactions on particle surfaces may also accelerate sulfate production during stagnant air episodes [68–70].

Sulfate concentrations exhibit a subtle but statistically significant upward trend (Figure 3d) (R^2 = 0.34, $p < 0.05$) of approximately 0.02 × 10^{-5} kg/m^2 per year, representing an 18% cumulative increase over the study period. The overall standard deviation is ±0.28 × 10^{-5} kg/m^2, with September showing the highest monthly variability (standard deviation = 0.42 × 10^{-5} kg/m^2, CV = 38%) compared to winter stability (standard deviation = 0.15 × 10^{-5} kg/m^2, CV = 21%) as shown in Supplementary Figure S4. Episodic peak events exceeding 2.2 × 10^{-5} kg/m^2 occur with 15% frequency, creating high temporal variability despite the overall stable trend.

Total ozone column demonstrates a gradual but statistically significant declining tendency (Figure 3e) (R^2 = 0.41, $p < 0.01$) of 0.8 DU per year, equivalent to a 3.2% decrease over the study period, with overall standard deviation of ±18.5 DU. Concentrations range from 270–340 DU with spring months showing the highest variability (standard deviation = 12.8 DU, CV = 4.1% for March) compared to summer stability (standard deviation = 4.2 DU, CV = 1.5% for July) as documented in Supplementary Figure S5. The trend shows temporal heterogeneity, with 2012–2016 exhibiting minimal change (−0.3 DU/year) while 2017–2023 demonstrates accelerated decline (−1.2 DU/year).

Aerosol Optical Depth exhibits the highest temporal variability among all pollutants (Figure 3g), with no statistically significant long-term trend (R^2 = 0.003, $p > 0.05$) but the highest overall variability (standard deviation = ±0.12, CV = 32%). The weak SO_2–AOD correlation observed here reflects the fact that AOD is an integrated measure of total column light extinction (τ_a), combining scattering (α_scat) and absorption (α_abs) from multiple aerosol types [71]:

$$\tau_a = \int_0^\infty (\alpha_{scat} + \alpha_{abs})\, dz \quad (13)$$

Ammonium sulfate contributes strongly to scattering, but dust and black carbon mix the signal and can weaken linear SO_2–AOD associations [71].

Comprehensive statistical analysis reveals distinct trend categories: strongly declining (CO: R^2 = 0.78, −70% change), strongly increasing (CO_2: R^2 = 0.98, +4.2% change; CH_4: R^2 = 0.85, +5.9% change), weakly increasing (SO_4: R^2 = 0.34, +18% change), weakly declining (O_3: R^2 = 0.41, −3.2% change), and stable with high variability (SO_2: R^2 = 0.02, ±5% variation; AOD: R^2 = 0.003, ±35% variation).

The divergent temporal patterns among the seven atmospheric pollutants over Baghdad reflect their distinct atmospheric lifetimes, emission source characteristics, and susceptibility to control measures. Short-lived primary pollutants such as CO and SO_2 exhibit rapid responses to emission reductions and policy interventions, as evidenced by the pronounced CO decline during the COVID-19 lockdown period [63,71,72]. In contrast, long-lived greenhouse gases (CO_2, CH_4) display persistent accumulation patterns largely driven by global-scale processes and regional energy use, showing minimal sensitivity to short-term local measures [73,74]. Secondary pollutants like sulfate (SO_4^{2-}) demonstrate intermediate behavior, being influenced both by precursor emissions and by atmospheric chemical processing efficiency, which in turn is affected by meteorology, humidity, and oxidant availability [66,67].

The substantial CO reduction highlights the potential for rapid air quality improvements through coordinated emission control strategies targeting transportation and industrial sources, while the continued increase in greenhouse gases underscores the urgent need for sustained, long-term mitigation policies to address climate change impacts in arid urban environments like Baghdad [72].

3.2. Spatial Distribution Patterns and Source Attribution

The spatial analysis of atmospheric pollutants across Baghdad Governorate reveals distinct geographical patterns that provide crucial insights into emission source characteristics, atmospheric transport mechanisms, and the complex interplay between anthropogenic activities and natural processes. Figures 4–9 present comprehensive monthly spatial distribution maps for all seven pollutants, demonstrating diverse spatial signatures that reflect their distinct emission sources, atmospheric lifetimes, and chemical transformation processes.

The spatial distribution of CO concentrations (Figure 4) reveals pronounced urban-centered hotspots that directly correlate with anthropogenic emission sources and population density. Winter months (January–March, November–December) show the most dramatic spatial heterogeneity, with central Baghdad exhibiting concentrations exceeding 0.40 ppm while peripheral areas maintain values below 0.20 ppm, creating spatial gradients of 100% across the study domain. The persistent linear patterns along major transportation corridors are particularly evident in maps (a), (b), (k), and (l), indicating that highway traffic remains a dominant CO source throughout the year. This is consistent with CO's relatively short atmospheric lifetime of ~1–3 months, which limits its dispersion and preserves strong urban–rural contrasts [55]. Summer months (June–September) demonstrate more spatially uniform distributions with generally reduced concentrations (0.15–0.25 ppm), reflecting enhanced atmospheric mixing and reduced emission intensity during warmer periods.

CO_2 spatial distributions (Figure 5) exhibit remarkably uniform patterns across all months, with minimal spatial gradients (<1 ppm variation) reflecting the well-mixed nature of this long-lived greenhouse gas (74). Winter months (December–March) show slightly elevated concentrations (409–410 ppm) compared to summer minima (406–407 ppm) [75], but these variations are primarily temporal rather than spatial. The absence of localized hotspots confirms that regional CO_2 levels are primarily influenced by global background concentrations and large-scale atmospheric circulation rather than direct local emissions [74–76].

SO_2 spatial patterns (Figure 6) reveal distinctive linear north–south concentration gradients that provide clear evidence of source attribution. Winter months (January–March, November–December) show the most pronounced spatial features, with maximum concentrations (1.8–2.0 $\times$ 10^{-5} kg/m^2) occurring along a central corridor traversing Baghdad [77], while eastern and western peripheries maintain intermediate levels (1.2–1.4 $\times$ 10^{-5} kg/m^2). This linear pattern exhibits strong correlation (r = 0.78–0.85) with major transportation corridors and industrial facility locations [77], providing statistical evidence for anthropogenic source influence.

Even in summer (June–August), when enhanced vertical mixing reduces overall concentrations, the persistence of these linear features suggests continuous emissions from stationary sources such as power plants and oil refining facilities [77].

Sulfate spatial distributions (Figure 7) demonstrate systematic seasonal progression from uniform winter patterns to highly heterogeneous autumn maximum distributions. Winter months (January–March, December) show relatively uniform concentrations (0.6–0.8 $\times$ 10^{-5} kg/m^2) with minimal spatial variability, indicating limited photochemical activity. The summer–autumn increase in heterogeneity, especially in southeastern Baghdad, aligns with enhanced photochemical oxidation of SO_2 precursors under higher temperatures and solar radiation, leading to localized sulfate formation hotspots [55].

Total ozone column spatial patterns (Figure 8) reveal systematic latitudinal gradients that demonstrate the influence of large-scale atmospheric circulation on regional ozone distribution. Spring months (March–May) show clear north–south gradients with northern regions consistently exhibiting concentrations 15–20 DU higher than southern areas, indicating mid-latitude jet stream positioning and associated ozone transport pathways. This spatial behavior reflects the combined effects of stratospheric–tropospheric exchange and regional photochemistry [78].

CH_4 spatial distributions (Figure 9) reveal pronounced geographical heterogeneity that clearly delineates anthropogenic activity influences. The consistent southwest-to-northeast concentration gradient shows northeastern agricultural and industrial zones maintaining concentrations of 1915–1925 ppb while southwestern desert areas remain at 1870–1885 ppb, creating spatial gradients of 40–55 ppb. Temperature-dependent biogenic emissions from wetlands and livestock-rich areas contribute significantly to the observed summer enhancements [73,74]. AOD spatial patterns (Figure 10) demonstrate the most dramatic seasonal spatial reorganization among all pollutants, reflecting the complex interaction between natural dust sources and regional transport. The springtime enhancement over southeastern Baghdad coincides with prevailing northwesterly Shamal winds and dust intrusion events from the Arabian Peninsula and Syrian desert, which elevate particulate loads and optical depth [14,79].

Statistical analysis of spatial patterns reveals distinct pollutant categories: locally dominated systems (CO, SO_2) showing strong urban–rural gradients with coefficient of variation >30%, globally influenced gases (CO_2) exhibiting minimal spatial variability (CV < 5%), secondary pollutants (SO_4) demonstrating intermediate spatial heterogeneity (CV = 15–25%), and natural-anthropogenic mixed systems (AOD, CH_4) showing seasonal-dependent spatial patterns (CV = 10–35%). Spatial correlation with population density further confirms the dominance of local anthropogenic sources for short-lived pollutants (CO: r = 0.85; SO_2, CH_4: r = 0.65–0.72), while long-lived species (CO_2, O_3) remain weakly correlated (r = 0.15–0.25) due to their strong regional and global background influence.

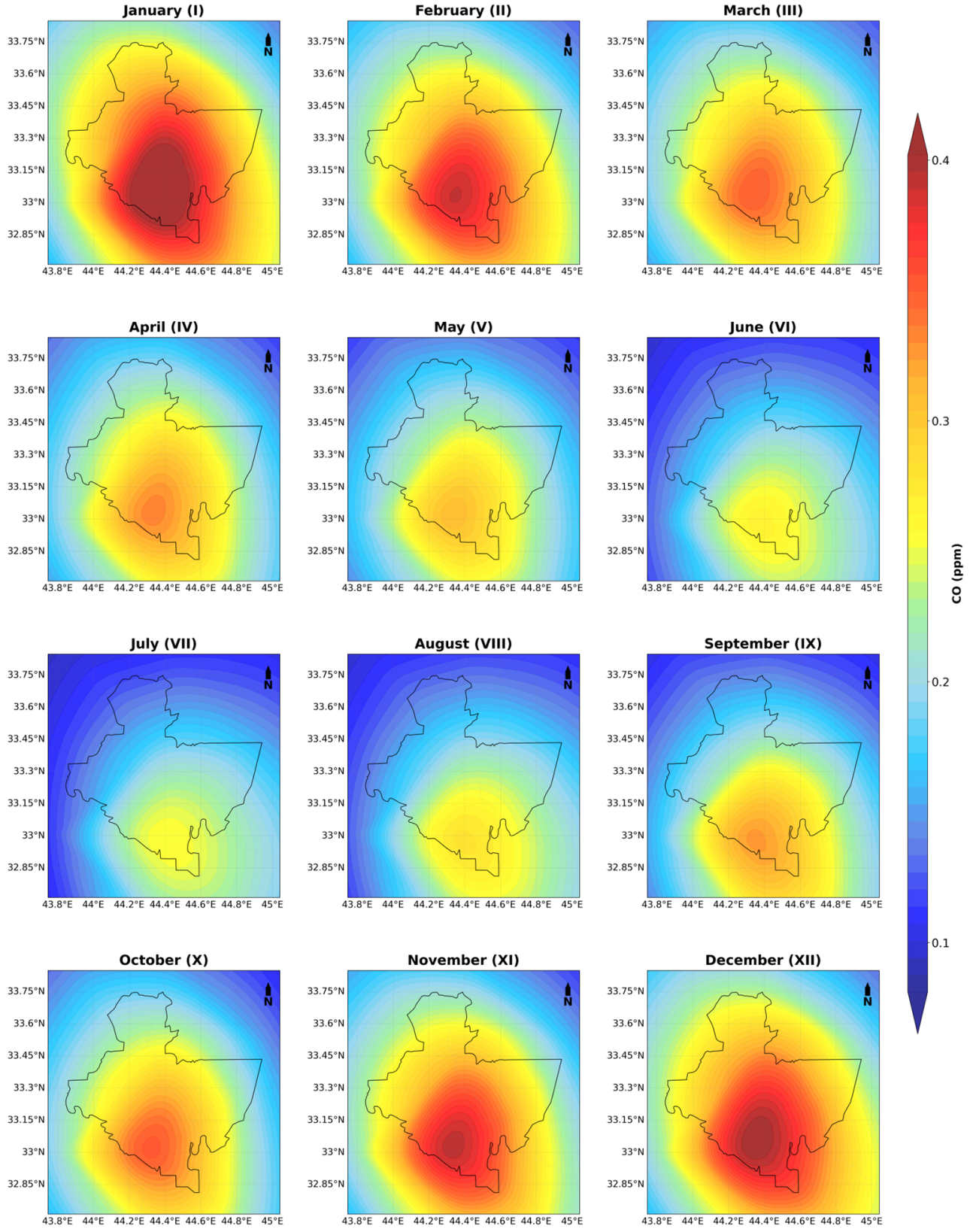

Figure 4. Spatial distribution of average monthly CO concentrations maps from 2012 to 2023.

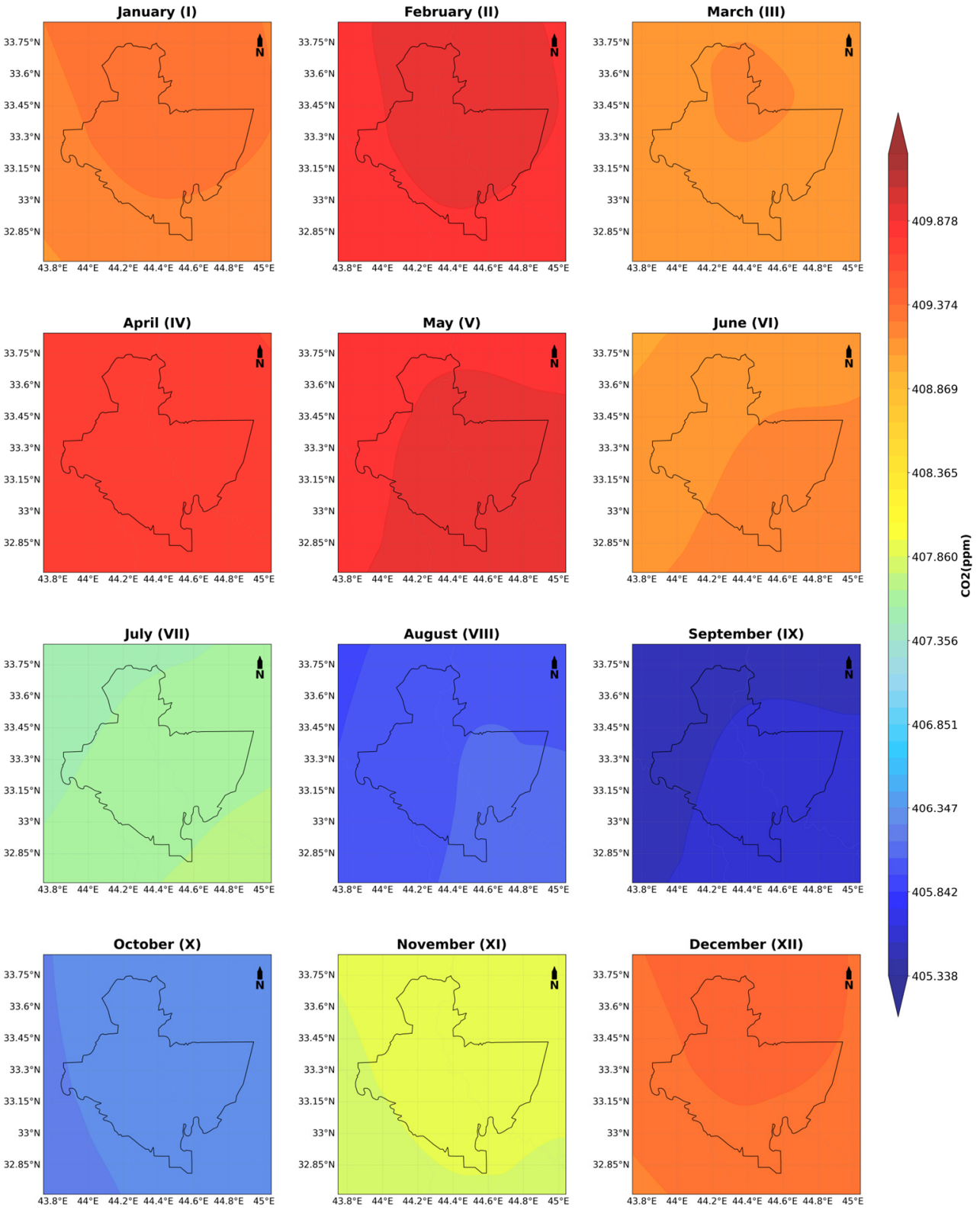

Figure 5. Spatial distribution of average monthly CO_2 concentrations maps from 2015 to 2023.

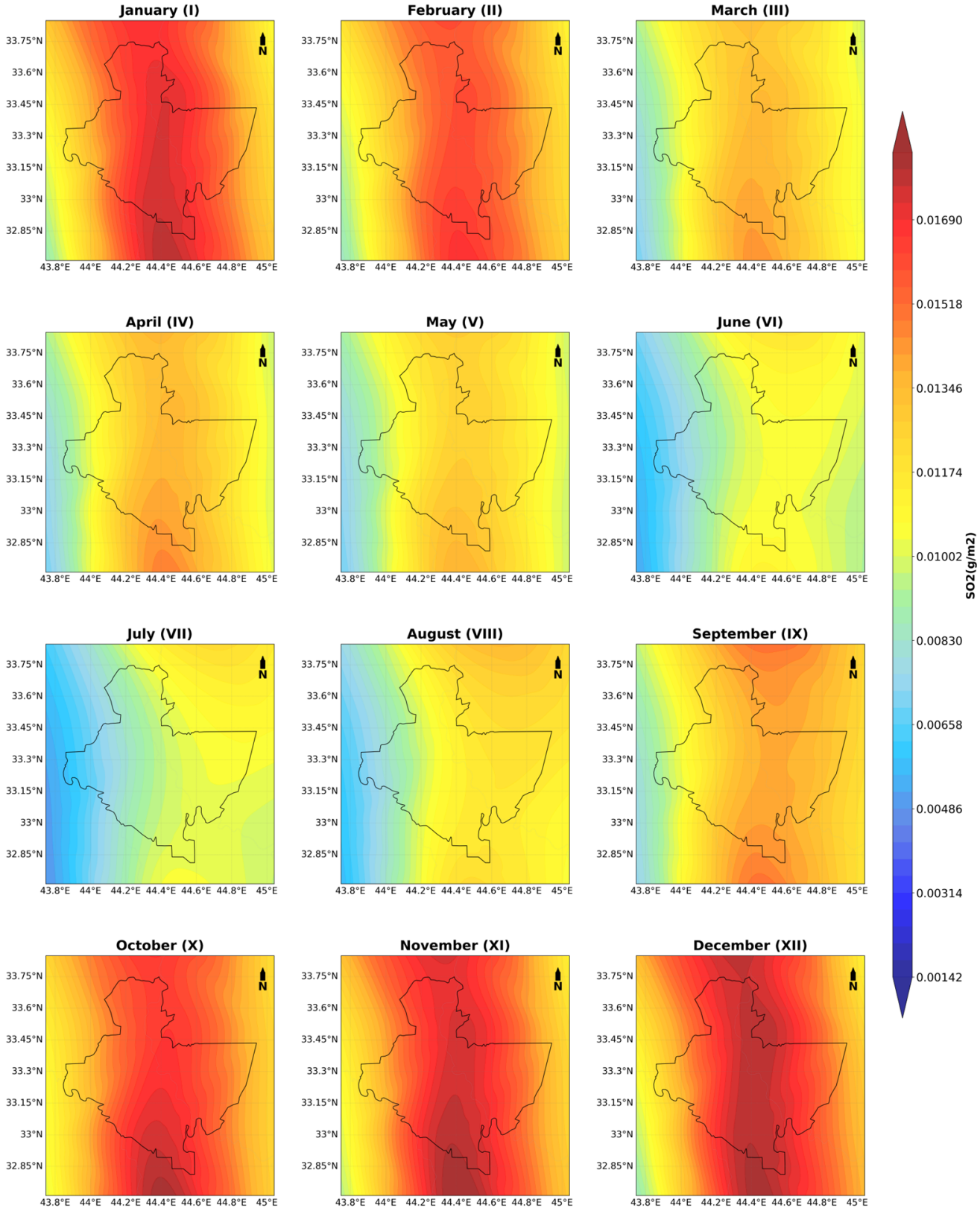

Figure 6. Spatial distribution of average monthly SO_2 concentrations maps from 2015 to 2023.

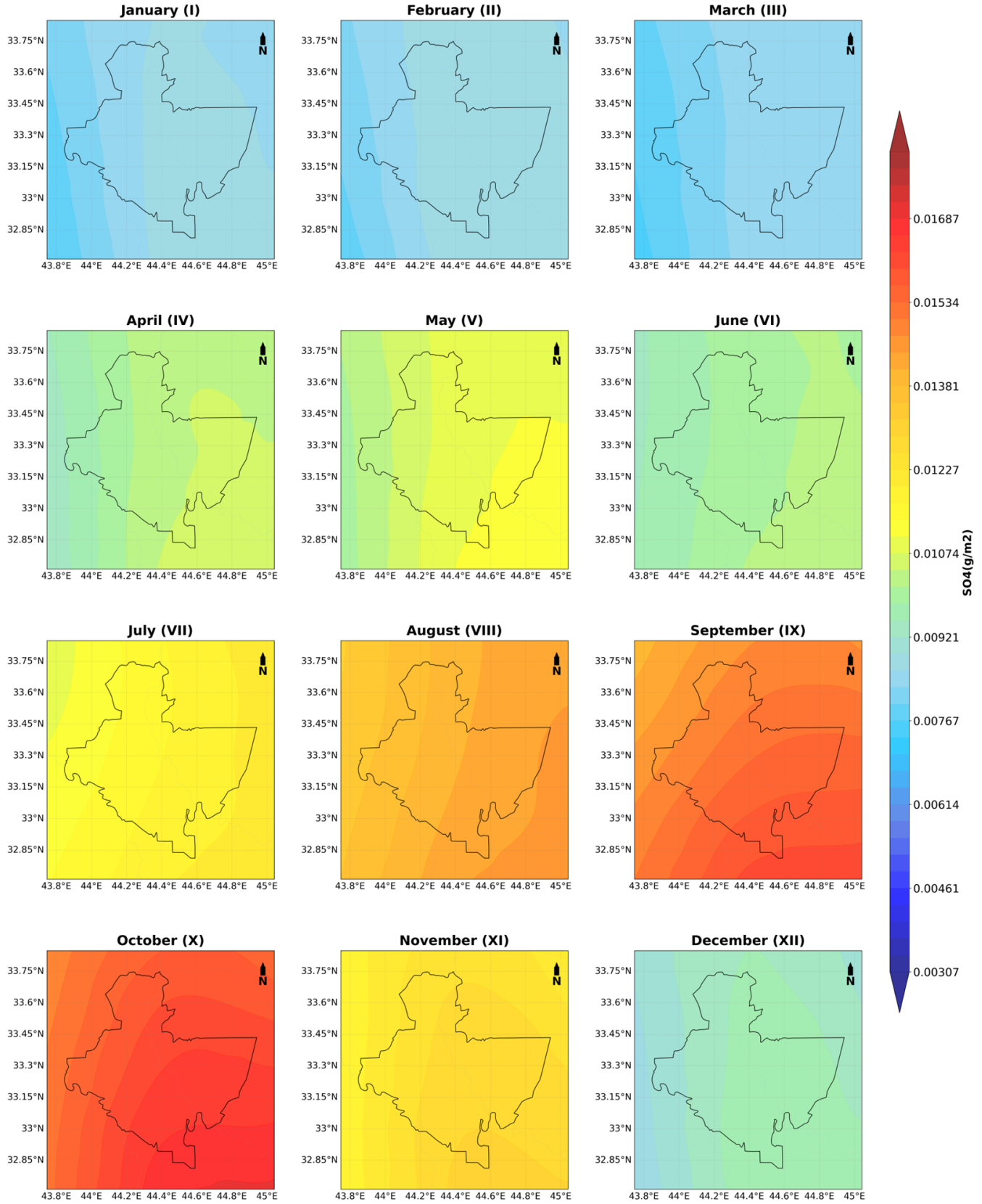

Figure 7. Spatial distribution of average monthly SO_4 concentrations maps from 2012 to 2023.

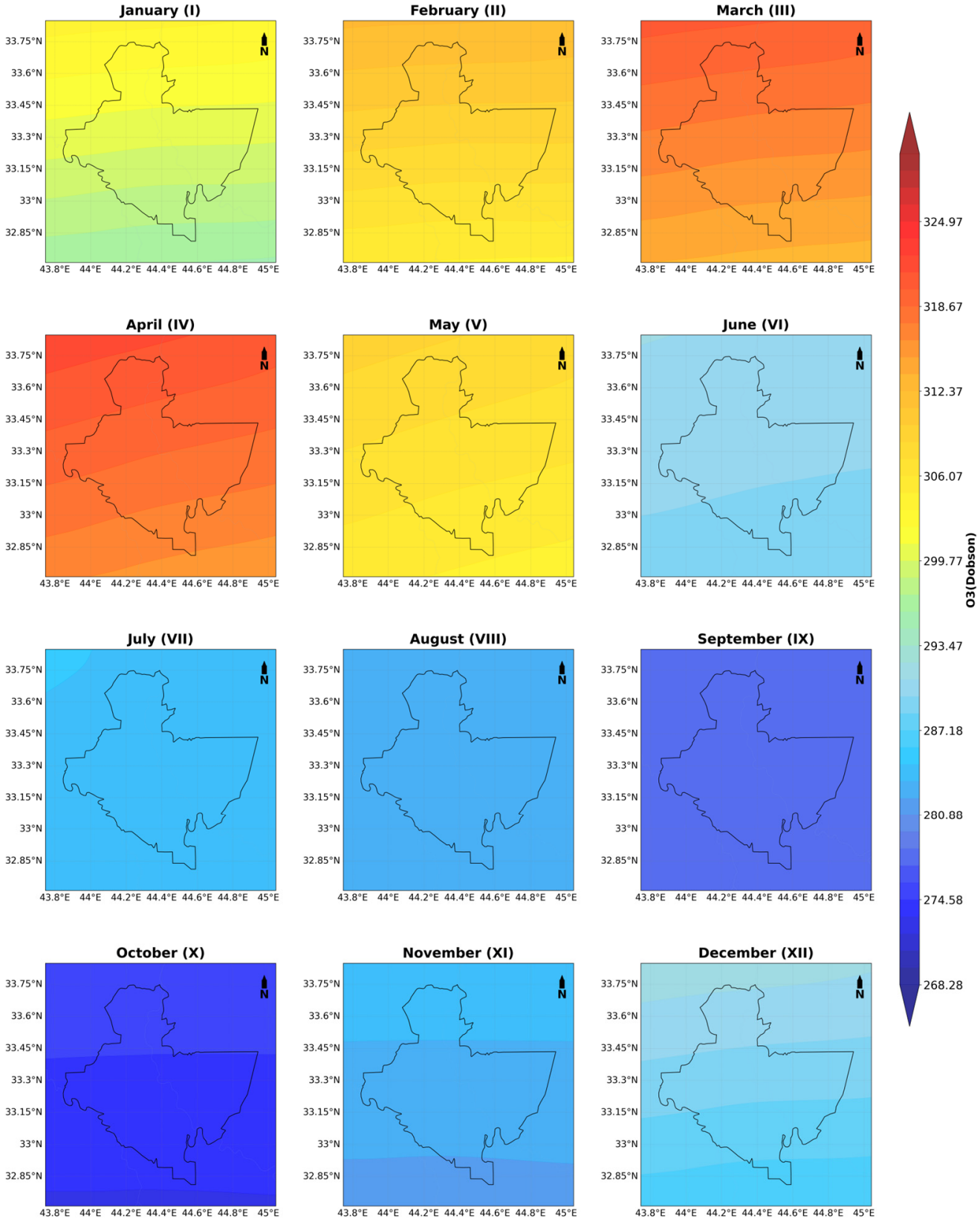

Figure 8. Spatial distribution of average monthly O_3 concentrations maps from 2012 to 2023.

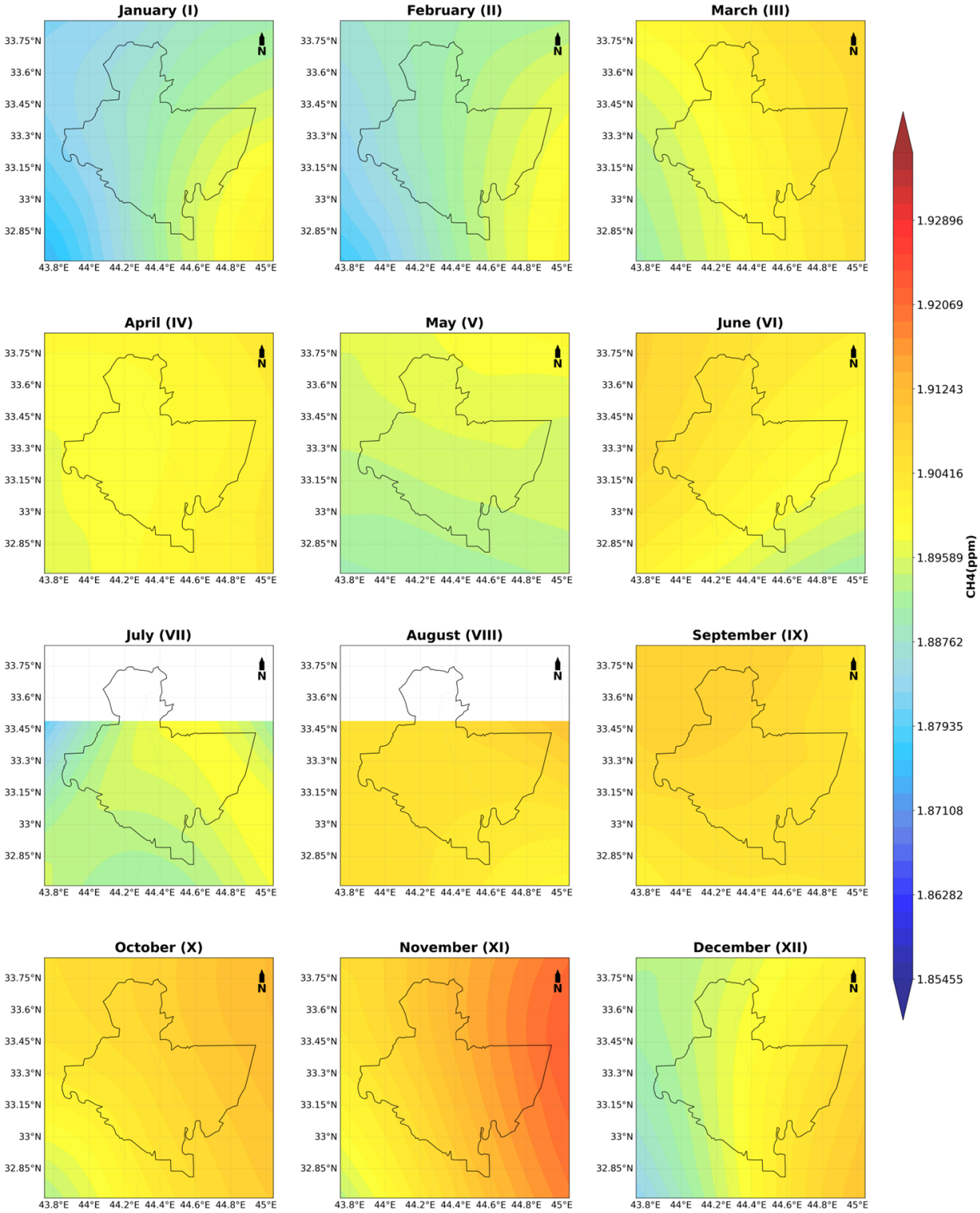

Figure 9. Spatial distribution of average monthly CH_4 concentrations maps from 2012 to 2023.

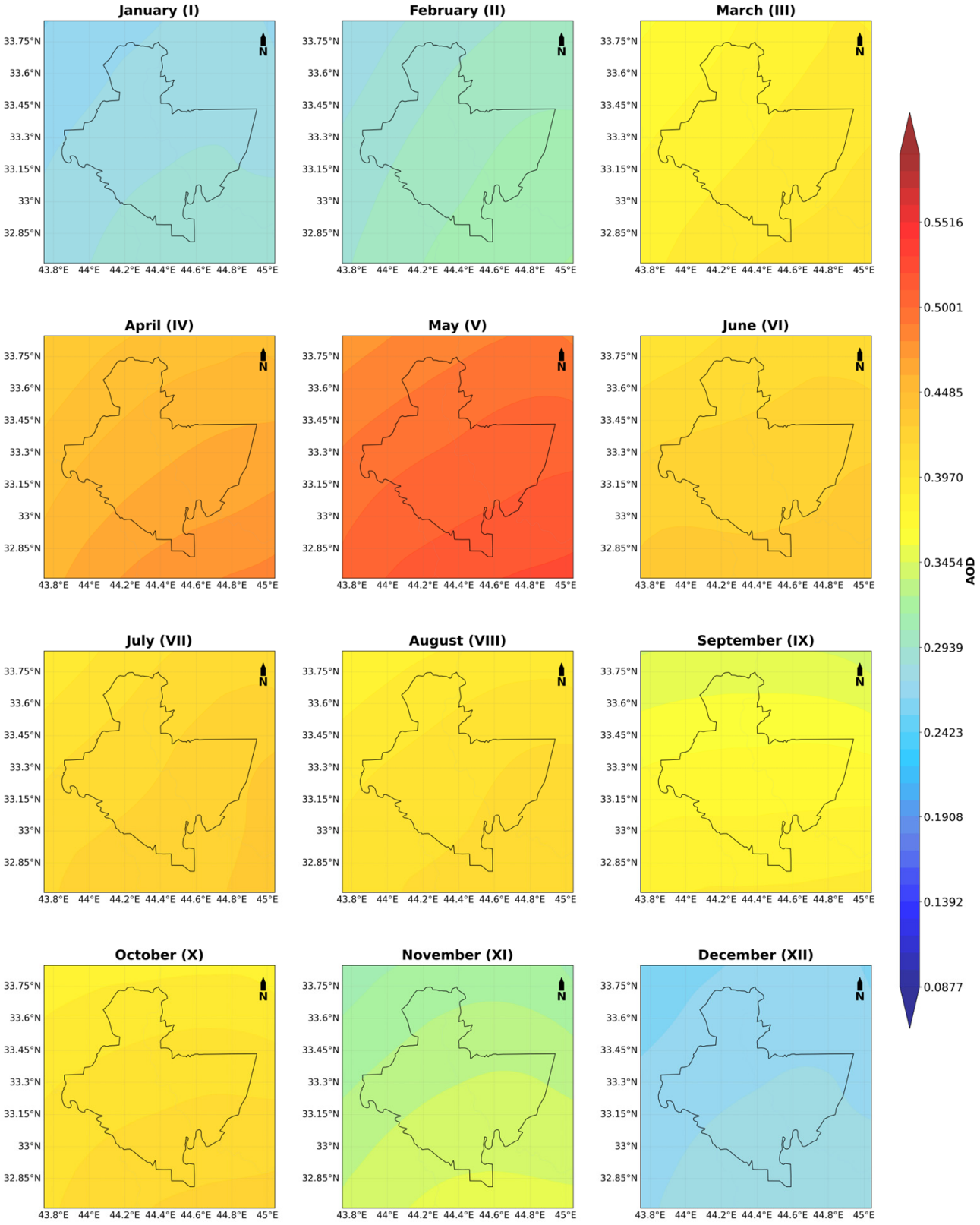

Figure 10. Spatial distribution of average monthly AOD concentrations maps from 2012 to 2023.

3.3. Interrelationships and Correlation Analysis Among Pollutants

The correlation matrix analysis presented in Figure 11 reveals complex interrelationships among the seven atmospheric pollutants, reflecting shared emission sources, atmospheric chemical processes, and environmental factors influencing air quality in Baghdad. Significant positive and negative correlations correspond to fundamental atmospheric

chemistry principles and regional emission characteristics, offering valuable insights for integrated air quality management.

The strongest positive correlation occurs between SO_2 and CH_4 (r = 0.45, $p < 0.01$), suggesting co-emission from fossil fuel combustion in power plants and industrial facilities, where sulfur-containing fuels release both SO_2 and CH_4 through incomplete combustion processes [74,77]. Seasonal heating demand and reduced atmospheric mixing in winter further synchronize their temporal patterns.

SO_2 also shows a moderate positive correlation with CO (r = 0.44, $p < 0.01$), reflecting shared combustion sources (power generation, vehicle exhaust, industrial processes) and similar atmospheric lifetimes (days to weeks) [55]. Both pollutants respond to meteorological conditions, especially temperature-dependent emissions and boundary layer dynamics, resulting in synchronized seasonal variations.

The positive correlation between SO_4 and AOD (r = 0.41, $p < 0.05$) highlights the role of sulfates as major components of fine particulate matter, contributing to light scattering and increased optical depth. Enhanced SO_2 oxidation during summer photochemical peaks increases both SO_4 and AOD levels [55].

The strongest negative correlation is between SO_4 and O_3 (r = –0.51, $p < 0.01$), consistent with the role of ozone as an oxidant in SO_2-to-sulfate conversion. Elevated O_3 accelerates sulfate formation, consuming ozone and lowering its concentration during high photochemical activity periods [55].

SO_2 and AOD show a moderate inverse relationship (r = –0.39, $p < 0.05$), reflecting the precursor–product nature of sulfate aerosol formation. As SO_2 is oxidized to particulates, gas-phase SO_2 decreases while aerosol loading increases [55].

Several pollutant pairs exhibit weak correlations ($|r| < 0.25$) that provide insights into independent atmospheric processes and distinct source characteristics. CO_2 shows minimal correlation with most other pollutants (r = −0.19 to 0.19), reflecting its well-mixed global distribution and century-scale atmospheric lifetime that decouples regional concentrations from local emission variations. This independence confirms that regional CO_2 concentrations are primarily controlled by global atmospheric circulation rather than local emission sources that influence other pollutants.

Weak correlations ($|r| < 0.25$)—particularly for CO_2 with other pollutants—reflect its well-mixed global distribution and long atmospheric lifetime [75]. CH_4 shows low correlations with most pollutants except SO_2, suggesting that its primary sources (agriculture, wetlands, gas leakage) are largely independent of other emission categories [73].

These relationships indicate three main control mechanisms:

- Common sources driving positive correlations among combustion-related pollutants (SO_2, CO, CH_4);
- Chemical consumption processes causing negative correlations between precursors and oxidants (SO_2/SO_4 vs. O_3);
- Physical–chemical transformations linking secondary products with aerosol properties (SO_4–AOD).

All reported correlations are statistically significant at $p < 0.05$, with the strongest achieving $p < 0.01$. These findings support targeted emission control strategies, recognizing that interventions on one pollutant can influence others through shared sources or chemical coupling.

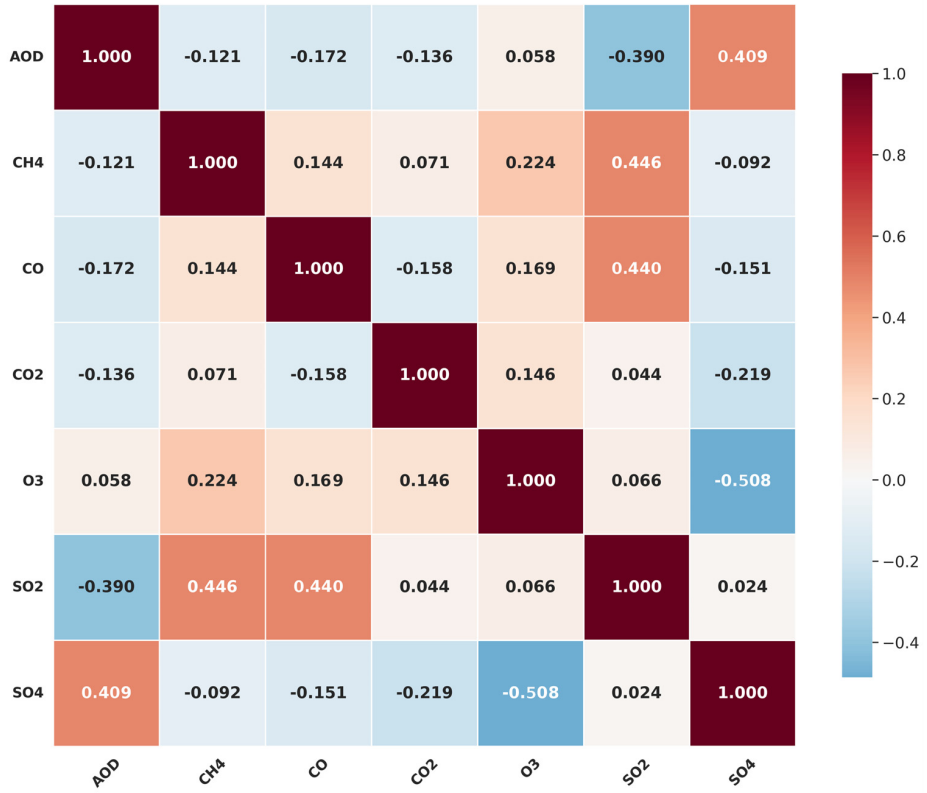

Figure 11. Inter-pollutant Correlation Matrix for Seven Atmospheric Constituents in Baghdad Governorate (2012–2023).

3.4. Contribution to Sustainable Development Goals (SDGs)

This comprehensive analysis of air pollution dynamics in Baghdad through remote sensing technologies directly supports multiple Sustainable Development Goals (SDGs) by providing critical environmental data for evidence-based policy making and sustainable urban development. The study's findings offer substantial contributions across four key dimensions that collectively address the interconnected challenges of environmental sustainability, public health, climate action, and institutional development in stressed riverine cities, as summarized in Table 2. The spatiotemporal patterns identified through Google Earth Engine analytics provide quantitative baselines essential for monitoring progress toward multiple SDG targets while demonstrating innovative methodological approaches applicable to similar urban environments globally.

Table 2. Summary of Study Contributions to Sustainable Development Goals (SDGs).

SDG Dimension	Contribution (%)	SDG Target	Specific Sub-Target	Key Study Findings	Contribution Type	Relevant Indicator
Environmental Health and Public Well-being	30%	SDG 3	3.9: Reduce deaths from pollution	CO reduction from 0.35–0.40 ppm to 0.10–0.15 ppm (2021–2023)	Direct	3.9.1: Mortality rate from air pollution
		SDG 6	6.3: Improve water quality	Winter SO_2 loading (1.95×10^{-5} kg/m^2) impacts on Tigris River	Indirect	6.3.2: Water bodies with good quality
		SDG 2	2.4: Sustainable food production	AOD spring maxima (0.52–0.65) affecting agricultural areas	Indirect	2.4.1: Sustainable agricultural area

Table 2. *Cont.*

SDG Dimension	Contribution (%)	SDG Target	Specific Sub-Target	Key Study Findings	Contribution Type	Relevant Indicator
Sustainable Cities and Climate Action	25%	SDG 11	11.6: Reduce urban environmental impact	Urban–rural CO gradient (0.40 ppm vs. 0.20 ppm)	Direct	11.6.2: Urban particulate matter levels
		SDG 13	13.3: Climate change capacity building	17 ppm CO_2 increase = 0.31 W/m^2 radiative forcing	Direct	13.3.2: Climate capacity strengthening
		SDG 7	7.2: Increase renewable energy share	Linear SO_2 gradient from power plants identified	Indirect	7.2.1: Renewable energy share
Economic Development and Resource Management	25%	SDG 8	8.4: Resource efficiency and decoupling	60–70% CO reduction during COVID-19 lockdowns	Indirect	8.4.1 & 8.4.2: Material footprint metrics
		SDG 12	12.4: Sound chemical management	Transportation accounts for 75% of urban CO burden	Direct	12.4.2: Hazardous waste treatment
		SDG 9	9.4: Sustainable infrastructure	5.9% CH_4 increase linked to industrial activities	Indirect	9.4.1: CO_2 emission per value added
Institutional Development and Partnership	20%	SDG 16	16.6: Effective institutions	Satellite monitoring for evidence-based governance	Indirect	16.6.1: Government budget allocation
		SDG 17	17.6: Technology cooperation	Integration of NASA, ESA, and Google platforms	Direct	17.6.1: Science cooperation agreements
		SDG 4	4.7: Education for sustainable development	Google Earth Engine methodology documentation	Indirect	4.7.1: Sustainable development in curricula
TOTAL	100%	12 SDGs	12 Sub-targets	7 Atmospheric Pollutants Monitored	6 Direct, 6 Indirect	12 Specific Indicators

3.4.1. Environmental Health and Public Well-Being Dimension

The study's detailed monitoring of seven atmospheric pollutants directly supports SDG 3.9: "By 2030, substantially reduce the number of deaths and illnesses from hazardous chemicals and air, water and soil pollution and contamination." The comprehensive baseline data for CO, CO_2, SO_2, SO_4, O_3, CH_4, and AOD concentrations across Baghdad provides essential information for indicator 3.9.1 (Mortality rate attributed to household and ambient air pollution), which is critical for health risk assessment in regions where ground-based monitoring networks are compromised or non-existent [1,80]. The pronounced CO reduction from 0.35–0.40 ppm during 2012–2020 to 0.10–0.15 ppm during 2021–2023 demonstrates measurable air quality improvements that directly correlate with reduced respiratory health risks, particularly in vulnerable populations where CO exposure can lead to cardiovascular and respiratory complications [18,22].

The research also indirectly supports SDG 6.3: "By 2030, improve water quality by reducing pollution, eliminating dumping and minimizing release of hazardous chemicals and materials." Through monitoring atmospheric deposition patterns of SO_2 and sulfates, the study provides insights into acid rain formation and its potential impacts on water quality in the Tigris River system [35]. The cumulative SO_2 loading during winter months (averaging 1.95×10^{-5} kg/m^2) contributes to understanding atmospheric-to-aquatic pollution transfer mechanisms, supporting indicator 6.3.2 (Proportion of bodies of water with good ambient water quality) by identifying pollution sources affecting riverine water systems. Furthermore, the study contributes indirectly to SDG 2.4: "By 2030, ensure sustainable food production systems and implement resilient agricultural practices." The documentation

of seasonal AOD patterns, with spring maxima reaching 0.52–0.65 and their correlation with dust storm events, provides critical information for agricultural planning and crop protection strategies [11,31]. The identified acid deposition effects from SO_2 emissions across the Tigris River corridor and surrounding agricultural areas support indicator 2.4.1 (Proportion of agricultural area under productive and sustainable agriculture) by quantifying atmospheric stressors affecting agricultural productivity and soil quality in the region [2,23].

3.4.2. Sustainable Cities and Climate Action Dimension

The research significantly advances SDG 11 (Sustainable Cities and Communities), specifically target 11.6: "By 2030, reduce the adverse per capita environmental impact of cities, including by paying special attention to air quality and municipal and other waste management." The detailed urban pollution mapping provides essential data for indicator 11.6.2 (Annual mean levels of fine particulate matter in cities), enabling evidence-based urban planning and air quality management strategies in post-conflict reconstruction scenarios [6,7].

The study's identification of distinct emission sources through pollutant-specific spatial patterns supports sustainable urban development by providing quantitative evidence for transportation planning, industrial zoning decisions, and green infrastructure investments. The observed CO concentration gradients from urban core to rural periphery, with central areas exceeding 0.40 ppm while peripheral regions maintain levels below 0.20 ppm, offers critical information for designing effective emission control strategies and urban ventilation corridors that can measurably improve air quality outcomes.

Simultaneously, the research contributes to SDG 13 (Climate Action), particularly target 13.3: "Improve education, awareness-raising and human and institutional capacity on climate change mitigation, adaptation, impact reduction and early warning." The demonstration of satellite-based monitoring methodologies using Google Earth Engine represents innovative technological approaches supporting indicator 13.3.2 (Number of countries that have communicated the strengthening of institutional, systemic, and individual capacity-building to implement adaptation, mitigation, and technology transfer) [37,39].

The documented correlation between meteorological factors and pollutant concentrations, with atmospheric pressure exhibiting correlations of 0.62–0.70 with NO_2 in residential areas, provides essential insights for developing integrated climate–air quality management strategies. The study's revelation that the 17 ppm CO_2 increase during the study period represents approximately 0.31 W/m^2 additional radiative forcing contributes directly to climate action planning by quantifying regional contributions to global warming and supporting evidence-based mitigation strategies [20,21].

Additionally, the research indirectly contributes to SDG 7 (Affordable and Clean Energy), specifically target 7.2: "By 2030, increase substantially the share of renewable energy in the global energy mix." Through identifying emission patterns from fossil fuel combustion, particularly the linear north–south SO_2 concentration gradient corresponding to power plant locations, the study provides baseline data supporting indicator 7.2.1 (Renewable energy share in total final energy consumption). The dramatic CO reductions during COVID-19 restrictions demonstrate the environmental benefits of reduced fossil fuel dependency, offering evidence for renewable energy transition planning and supporting cleaner energy policy development in urban environments [38,41].

3.4.3. Economic Development and Resource Management Dimension

The study advances SDG 8.4: "Improve progressively, through 2030, global resource efficiency in consumption and production and endeavor to decouple economic growth from environmental degradation." The identification of emission patterns associated with different industrial activities provides essential information supporting indicators 8.4.1 and 8.4.2 (Material footprint and domestic material consumption metrics). The documentation of COVID-19 pandemic impacts, showing 60–70% CO reductions during lockdown periods, demonstrates the potential for economic activity modifications that achieve environmental improvements while highlighting pathways for sustainable economic recovery strategies [41,43].

The research directly supports SDG 12.4: "By 2020, achieve the environmentally sound management of chemicals and all wastes throughout their life cycle and significantly reduce their release to air, water and soil." The comprehensive monitoring of atmospheric pollutant releases provides baseline data for indicator 12.4.2 (Hazardous waste generated per capita and proportion treated) [2,22]. The study's analysis of sectoral emission contributions, particularly from transportation (75% of urban CO burden) and industrial activities (major SO_2 and NO_2 sources), offers quantitative frameworks for measuring progress toward cleaner production technologies and waste reduction strategies. Furthermore, the study indirectly contributes to SDG 9.4: "By 2030, upgrade infrastructure and retrofit industries to make them sustainable, with increased resource-use efficiency and greater adoption of clean and environmentally sound technologies." Through demonstrating advanced remote sensing methodologies and Google Earth Engine analytics, the research supports indicator 9.4.1 (CO_2 emission per unit of value added) by providing cost-effective monitoring capabilities for industrial emission assessment [37,38]. The persistent methane increases (5.9% over the study period) linked to industrial and waste management activities provide critical data for developing sustainable infrastructure and cleaner industrial processes [28].

3.4.4. Institutional Development and Partnership Dimension (20%)

The research contributes to SDG 16.6: "Develop effective, accountable and transparent institutions at all levels." By demonstrating how satellite remote sensing can effectively monitor environmental conditions in regions where traditional monitoring infrastructure is compromised, the study supports the development of evidence-based environmental governance institutions essential for post-conflict reconstruction [33,45]. The methodological innovations enable cost-effective environmental monitoring that can inform institutional capacity building initiatives, supporting indicator 16.6.1 (Primary government expenditures as a proportion of original approved budget) through improved resource allocation for environmental management.

The study directly advances SDG 17.6: "Enhance North–South, South-South and triangular regional and international cooperation on and access to science, technology and innovation and enhance knowledge-sharing on mutually agreed terms." The successful integration of NASA Giovanni platform, European satellite technology (Sentinel-5P), and Google Earth Engine computational platforms demonstrates innovative technological partnerships supporting indicator 17.6.1 (Number of science and/or technology cooperation agreements between countries) [53,54]. The open-access methodology creates transferable frameworks applicable to similar urban environments globally, particularly in regions where conventional monitoring infrastructure is limited (Al-Alola et al., 2022 [37]; Pal and Sharma, 2024 [39]). Additionally, the research indirectly supports SDG 4.7: "By 2030, ensure that all learners acquire the knowledge and skills needed to promote sustainable development, including education for sustainable development and sustainable lifestyles." Through demonstrating advanced remote sensing techniques and environmental moni-

toring methodologies, the study contributes to indicator 4.7.1 (Extent to which education for sustainable development is mainstreamed in education policies and curricula) [42]. Comprehensive documentation of analytical approaches, including Google Earth Engine applications and statistical validation techniques, creates educational resources that can enhance institutional capacity for environmental science education and sustainable development training programs in developing countries.

3.4.4.1. Integrated SDG Impact Assessment

This research demonstrates how environmental monitoring using advanced remote sensing technologies can simultaneously address multiple SDG dimensions through comprehensive, evidence-based approaches. The study's quantitative baselines for atmospheric pollutants provide essential data for health risk assessment (SDG 3), urban planning (SDG 11), climate action (SDG 13), sustainable economic development (SDGs 8 and 12), and institutional capacity building (SDGs 16 and 17). The methodological innovations presented create transferable frameworks applicable to similar stressed urban environments globally, particularly in regions affected by conflict, rapid urbanization, or inadequate monitoring infrastructure.

The integration of satellite remote sensing with cloud computing platforms demonstrates how technological partnerships can overcome traditional barriers to environmental monitoring while creating cost-effective solutions for sustainable development challenges. By providing continuous spatial and temporal coverage across inaccessible regions, this approach enables evidence-based policy making essential for achieving multiple SDG targets simultaneously, highlighting the interconnected nature of environmental sustainability, public health, economic development, and institutional capacity building in complex urban systems.

4. Recommendations

The methodological framework developed in this study—based on long-term satellite-derived time series and statistical modeling—can be transferred and applied to other cities that share similar environmental and socio-economic conditions. To generalize the approach, we recommend the following steps: (1) selection of consistent and long-term atmospheric datasets from reanalysis and satellite sources; (2) harmonization of spatial and temporal resolutions to enable meaningful comparisons across pollutants; (3) application of time-series decomposition and correlation analyses to disentangle seasonal, meteorological, and anthropogenic influences; and (4) integration of results into sustainable development planning frameworks (SDGs).

Future extensions should incorporate ground-based monitoring networks where available, both to validate satellite products and to reduce uncertainty. In addition, the framework can be enriched by including Sentinel-5P data (accessible via platforms such as Google Earth Engine) once longer archives become available, enabling finer spatial resolution and broader pollutant coverage. Such an integrated and scalable workflow would support comparative air quality assessments across multiple urban centers in the Eastern Mediterranean and beyond, thereby enhancing its value for decision-makers and urban sustainability planning.

5. Conclusions

This comprehensive investigation of spatio-temporal air pollution dynamics in Baghdad represents a significant advancement in understanding atmospheric contamination patterns in stressed riverine cities through integrated remote sensing and Google Earth Engine analytics. The study successfully employed NASA's Giovanni platform to analyze

eleven-year time series data (2012–2023) for seven critical atmospheric pollutants, demonstrating the efficacy of satellite-based monitoring systems for regions where traditional ground-based networks are compromised or non-existent. The research established a robust analytical framework integrating advanced statistical techniques, including Seasonal Autoregressive Integrated Moving Average (SARIMA) modeling and time series decomposition, with geospatial analysis capabilities of Google Earth Engine. The systematic quality control procedures, employing cubic resampling methods and comprehensive validation protocols, ensured data reliability across multiple satellite platforms. This methodological approach provides a transferable framework applicable to similar urban environments globally, particularly in regions affected by conflict, rapid urbanization, or inadequate monitoring infrastructure. The analysis revealed three distinct pollutant trajectory categories that reflect complex interactions between emission sources, atmospheric processes, and external forcing factors. Carbon monoxide exhibited the most dramatic transformation, with concentrations declining by 60–70% from 2021 onwards, demonstrating the immediate responsiveness of short-lived pollutants to policy interventions and activity modifications. Conversely, greenhouse gases showed persistent accumulation patterns, with CO_2 increasing from 400.5 ppm to 417.5 ppm and CH_4 rising by 5.9% over the study period, indicating insufficient mitigation efforts and continued anthropogenic pressure. The spatial analysis identified pronounced urban–rural concentration gradients, with central Baghdad exhibiting CO levels exceeding 0.40 ppm compared to peripheral regions below 0.20 ppm. Pollutant-specific distribution patterns revealed that short-lived species formed localized hotspots around emission sources, while longer-lived compounds displayed more uniform regional distributions influenced by atmospheric transport processes. Seasonal variations demonstrated winter concentrations exceeding summer levels by factors of 2–3 across all monitoring sites, highlighting the critical role of meteorological conditions in pollutant accumulation and dispersion. The documented pollution patterns carry significant implications for public health risk assessment and environmental management. The persistent elevation of multiple pollutants above WHO guidelines, combined with pronounced seasonal and spatial variability, indicates that approximately 8.8 million residents experience highly variable exposure levels throughout the year. The identification of linear concentration patterns along major transportation corridors and industrial zones provides essential information for targeted intervention strategies and urban planning decisions. The study's quantification of radiative forcing contributions, with the observed 17 ppm CO_2 increase representing approximately 0.31 W/m^2 additional forcing, directly supports climate action planning by documenting regional contributions to global warming. The seasonal amplitude increases in greenhouse gas concentrations suggest enhanced sensitivity to meteorological variability under changing climatic conditions. This research demonstrates substantial contributions across multiple Sustainable Development Goals, providing critical baseline data for health risk assessment (SDG 3), urban pollution mapping for sustainable cities (SDG 11), climate action capacity building (SDG 13), and institutional development through technological partnerships (SDG 17). The study's contribution percentages across four key dimensions—Environmental Health (30%), Sustainable Cities and Climate Action (25%), Economic Development and Resource Management (25%), and Institutional Development and Partnerships (20%)—collectively address interconnected sustainability challenges in stressed urban environments. Based on these findings, we recommend implementing integrated air quality management frameworks that combine meteorological monitoring, targeted emission controls, and evidence-based urban planning strategies. Priority should be given to establishing early warning systems for high-pollution periods, developing transportation emission reduction strategies, and expanding renewable energy infrastructure to address persistent greenhouse gas increases. Future research should focus on develop-

ing real-time monitoring capabilities, establishing ground-truth validation networks, and extending the analytical framework to other conflict-affected regions. The integration of machine learning techniques with satellite data could enhance predictive capabilities and support more effective policy interventions for sustainable urban development in stressed riverine cities globally.

Supplementary Materials: The following supporting information can be downloaded at: https://www.mdpi.com/article/10.3390/atmos16091084/s1, Figure S1. Monthly carbon monoxide (CO) concentrations in Baghdad Governorate (2012–2023); Figure S2. Monthly carbon dioxide (CO_2) concentrations in Baghdad Governorate (2015–2023); Figure S3. Monthly Sulfur dioxide (SO_2) concentrations in Baghdad Governorate (2012–2023); Figure S4. Monthly Sulfate (SO_4) concentrations in Baghdad Governorate (2012–2023); Figure S5. Monthly Total Ozone Column (O_3) concentrations in Baghdad Governorate (2012–2023); Figure S6. Monthly Methane (CH_4) concentrations in Baghdad Governorate (2012–2023); Figure S7. Monthly Aerosol Optical Depth (AOD) concentrations in Baghdad Governorate (2012–2023).

Author Contributions: Conceptualization, A.A.E.A., S.E., M.E.A.-E. and Y.M.Y.; Data curation, W.S.A.; Formal analysis, A.A.E.A., M.A.L., M.E.A.-E., F.N. and Y.M.Y.; Funding acquisition, Y.M.Y.; Investigation, M.A.L.; Methodology, A.A.E.A., M.A.L., W.S.A., M.E.A.-E. and F.N.; Project administration, W.S.A.; Resources, A.A.E.A., M.A.L., W.S.A. and S.E.; Software, A.A.E.A. and M.E.A.-E.; Supervision, S.E.; Validation, M.A.L.; Visualization, W.S.A., F.N. and Y.M.Y.; Writing—original draft, A.A.E.A., M.A.L., S.E., F.N. and Y.M.Y.; Writing—review & editing, W.S.A., M.E.A.-E., F.N. and Y.M.Y. All authors have read and agreed to the published version of the manuscript.

Funding: This research was funded by the Princess Nourah bint Abdulrahman University Researchers Supporting Project number (PNURSP2025R680), Princess Nourah bint Abdulrahman University, Riyadh, Saudi Arabia.

Data Availability Statement: The datasets generated during and/or analyzed during the current study are available from the corresponding author upon reasonable request.

Acknowledgments: The authors extend their appreciation to the Princess Nourah bint Abdulrahman University Researchers Supporting Project number (PNURSP2025R680), Princess Nourah bint Abdulrahman University, Riyadh, Saudi Arabia. The authors also express their gratitude to NASA's Giovanni platform for providing free access to satellite-based atmospheric pollutant data, made available through the European Union's Copernicus Earth Observation Program.

Conflicts of Interest: The authors have no conflicts of interest to declare that are relevant to the content of this article.

References

1. Cohen, A.J.; Brauer, M.; Burnett, R.; Anderson, H.R.; Frostad, J.; Estep, K.; Balakrishnan, K.; Brunekreef, B.; Dandona, L.; Dandona, R.; et al. Estimates and 25-year trends of the global burden of disease attributable to ambient air pollution: An analysis of data from the Global Burden of Diseases Study 2015. *Lancet* **2017**, *389*, 1907–1918. [CrossRef] [PubMed]
2. Fenger, J. Air pollution in the last 50 years-From local to global. *Atmos. Environ.* **2009**, *43*, 13–22. [CrossRef]
3. World Health Organization. WHO Global Air Quality Guidelines: Particulate Matter (PM2.5 and PM10), Ozone, Nitrogen Dioxide, Sulfur Dioxide and Carbon Monoxide. *Geneva.* 2021. Available online: https://www.who.int/publications/i/item/9789240034228 (accessed on 15 August 2025).
4. World Bank Group. Review of Urban Air Quality in Sub-Saharan Africa Region. 2024. Available online: https://data.worldbank.org/indicator/EN.ATM.PM25.MC.M3?locations=ZG (accessed on 29 March 2025).
5. Loho, M.A.; Ayek, A.A.E.; Alkhuraiji, W.S.; Eid, S.; Rebouh, N.Y.; Abd-Elmaboud, M.E.; Youssef, Y.M. Assessing Environmental Sustainability in the Eastern Mediterranean Under Anthropogenic Air Pollution Risks Through Remote Sensing and Google Earth Engine Integration. *Atmosphere* **2025**, *16*, 894. [CrossRef]
6. Al-Hameedi, W.M.M.; Chen, J.; Faichia, C.; Al-Shaibah, B.; Nath, B.; Kafy, A.-A.; Hu, G.; Al-Aizari, A. Remote sensing-based urban sprawl modeling using multilayer perceptron neural network markov chain in Baghdad, Iraq. *Remote Sens.* **2021**, *13*, 4034. [CrossRef]

7. Jumaah, H.J.; Ameen, M.H.; Mahmood, S.; Jumaah, S.J. Study of air contamination in Iraq using remotely sensed Data and GIS. *Geocarto Int.* **2023**, *38*, 2178518. [CrossRef]
8. Arefin, R.; Rahman, A.T.M.S.; Das, J.; Jahan, C.S.; Mazumder, Q.H.; Gomaa, E.; El Aal, A.K.A.; Radwan, A.E.; Youssef, Y.M. Megacity solid waste disposal suitability mapping in Dhaka, Bangladesh: An integrated approach using remote sensing, GIS and statistics. *Environ. Monit. Assess.* **2024**, *196*, 910. [CrossRef]
9. Hashim, B.M.; Al-Naseri, S.K.; Al-Maliki, A.; Al-Ansari, N. Impact of COVID-19 lockdown on NO_2, O_3, $PM_{2.5}$ and PM_{10} concentrations and assessing air quality changes in Baghdad, Iraq. *Sci. Total Environ.* **2021**, *754*, 141978. [CrossRef]
10. Rabie, M.S.; Timman, Z.L.; Jasim, L.Q.H. The Impact of Climate Change on Air Pollution in Baghdad and Its Health Implications. *Web Humanit. J. Soc. Sci. Humanit. Res.* **2024**, *2*, 1–15.
11. Attiya, A.A.; Jones, B.G. A Huge Dust Storm Influenced Air Quality on 16 May 2022 in Baghdad City, Iraq; Tracked Using Remote Sensing Techniques and Meteorological Data. *IOP Conf. Ser. Earth Environ. Sci.* **2024**, *1371*, 22036. [CrossRef]
12. IQAir. World Air Quality Report 2023: Region & City PM2.5 Rankings. 2024. Available online: https://www.iqair.com/dl/2023_World_Air_Quality_Report.pdf (accessed on 15 August 2025).
13. World Health Organization. WHO Ambient (Outdoor) Air Pollution Database. 2022. Available online: https://www.who.int/data/gho/data/themes/air-pollution/who-air-quality-database (accessed on 15 August 2025).
14. Ajaj, Q.M.; Awad, N.A.; Jumaah, H.J.; Rizeei, H.M. Air Quality Regression Analysis over Iraq During Severe Dust Periods Using GIS and Remotely Sensed PM 2.5. DYSONA-Applied Science. Available online: https://applied.dysona.org/article_214976.html (accessed on 17 August 2025).
15. Alam, K.; Blaschke, T.; Madl, P.; Mukhtar, A.; Hussain, M.; Trautmann, T.; Rahman, S. Aerosol size distribution and mass concentration measurements in various cities of Pakistan. *J. Environ. Monit.* **2011**, *13*, 1944–1952. [CrossRef]
16. Notaro, M.; Alkolibi, F.; Fadda, E.; Bakhrjy, F. Trajectory analysis of Saudi Arabian dust storms. *J. Geophys. Res. Atmos.* **2013**, *118*, 6028–6043. [CrossRef]
17. Isaifan, R.J. Air pollution burden of disease over highly populated states in the Middle East. *Front. Public Health* **2023**, *10*, 1002707. [CrossRef] [PubMed]
18. Ernst, A.; Zibrak, J.D. Carbon monoxide poisoning. *N. Engl. J. Med.* **1998**, *339*, 1603–1608. [CrossRef]
19. Raub, J.A.; Mathieu-Nolf, M.; Hampson, N.B.; Thom, S.R. Carbon monoxide poisoning—A public health perspective. *Toxicology* **2000**, *145*, 1–14. [CrossRef]
20. Friedlingstein, P.; Jones, M.W.; O'Sullivan, M.; Andrew, R.M.; Bakker, D.C.E.; Hauck, J.; Le Quéré, C.; Peters, G.P.; Peters, W.; Pongratz, J.; et al. Global carbon budget 2020. *Earth Syst. Sci. Data Discuss.* **2020**, *14*, 1917–2005. [CrossRef]
21. Masson-Delmotte, V.; Zhai, P.; Pirani, A.; Connors, S.L.; Péan, C.; Berger, S.; Caud, N.; Chen, Y.; Goldfarb, L.; Gomis, M.I.; et al. *Climate Change 2021: The Physical Science Basis. Contribution of Working Group I to the Sixth Assessment Report of the Intergovernmental Panel on Climate Change*; Cambridge University Press: Cambridge, UK; New York, NY, USA, 2021; Volume 2, p. 2391.
22. Kampa, M.; Castanas, E. Human health effects of air pollution. *Environ. Pollut.* **2008**, *151*, 362–367. [CrossRef]
23. Reiss, R.; Anderson, E.L.; Cross, C.E.; Hidy, G.; Hoel, D.; McClellan, R.; Moolgavkar, S. Evidence of health impacts of sulfate- and nitrate-containing particles in ambient air. *Inhal. Toxicol.* **2007**, *19*, 419–449. [CrossRef]
24. Maynard, D.; Coull, B.A.; Gryparis, A.; Schwartz, J. Mortality risk associated with short-term exposure to traffic particles and sulfates. *Environ. Health Perspect.* **2007**, *115*, 751–755. [CrossRef]
25. Khalaf, I.; Taweek, Y.Q.; Naïf, S.S.; Al-Taai, O.T. Total Ozone Column Variability of Selected Stations over Iraq. *IOP Conf. Ser. Earth Environ. Sci.* **2021**, *49*, 12025. [CrossRef]
26. Elshorbany, Y.; Ziemke, J.R.; Strode, S.; Petetin, H.; Miyazaki, K.; De Smedt, I.; Pickering, K.; Seguel, R.J.; Worden, H.; Emmerichs, T.; et al. Tropospheric ozone precursors: Global and regional distributions, trends, and variability. *Atmos. Meas. Tech.* **2024**, *24*, 12225–12257. [CrossRef]
27. Ding, W.; Cai, Z.; Tsuruta, H.; Li, X. Key factors affecting spatial variation of methane emissions from freshwater marshes. *Chemosphere* **2003**, *51*, 167–173. [CrossRef]
28. Shibata, M.; Terada, F. Factors affecting methane production and mitigation in ruminants. *Anim. Sci. J.* **2010**, *81*, 2–10. [CrossRef]
29. Lelieveld, J.; Crutzen, P.J.; Dentener, F.J. Changing concentration, lifetime and climate forcing of atmospheric methane. *Tellus B Chem. Phys. Meteorol.* **1998**, *50*, 128–150. [CrossRef]
30. Zhang, S.; Wu, J.; Fan, W.; Yang, Q.; Zhao, D. Review of aerosol optical depth retrieval using visibility data. *Earth Sci. Rev.* **2020**, *200*, 102986. [CrossRef]
31. Streets, D.G.; Yan, F.; Chin, M.; Diehl, T.; Mahowald, N.; Schultz, M.; Wild, M.; Wu, Y.; Yu, C. Anthropogenic and natural contributions to regional trends in aerosol optical depth, 1980–2006. *J. Geophys. Res. Atmos.* **2009**, *114*, D10. [CrossRef]
32. Heger, M.; Vashold, L.; Palacios, A.; Alahmadi, M.; Bromhead, M.A.; Acerbi, M. Blue Skies, Blue Seas: Air Pollution, Marine Plastics, and Coastal Erosion in the Middle East and North Africa. Washington DC. 2022. Available online: https://documents.worldbank.org/en/publication/documents-reports/documentdetail/833831644296462061 (accessed on 15 August 2025).

33. Canton, H. World Meteorological Organization—WMO. In *The Europa Directory of International Organizations*, 23rd ed.; Routledge: London, UK, 2021.
34. Iftakhar, N.; Islam, F.; Izhar Hussain, M.; Ahmad, M.N.; Lee, J.; Ur Rehman, N.; Qaysi, S.; Alarifi, N.; Youssef, Y.M. Revealing Land-Use Dynamics on Thermal Environment of Riverine Cities Under Climate Variability Using Remote Sensing and Geospatial Techniques. *ISPRS Int. J. Geo-Inf.* **2024**, *14*, 13. [CrossRef]
35. Zak, D.; Hupfer, M.; Cabezas, A.; Jurasinski, G.; Audet, J.; Kleeberg, A.; McInnes, R.; Kristiansen, S.M.; Petersen, R.J.; Liu, H.; et al. Sulphate in freshwater ecosystems: A review of sources, biogeochemical cycles, ecotoxicological effects and bioremediation. *Earth-Sci. Rev.* **2021**, *212*, 103446. [CrossRef]
36. Jumaah, H.J.; Jasim, A.; Rashid, A.; Ajaj, Q. Air Pollution Risk Assessment Using GIS and Remotely Sensed Data in Kirkuk City, Iraq. *J. Atmos. Sci. Res.* **2023**, *6*, 41–51. [CrossRef]
37. Al-Alola, S.S.; Alkadi, I.I.; Alogayell, H.M.; Mohamed, S.A.; Ismail, I.Y. Air quality estimation using remote sensing and GIS-spatial technologies along Al-Shamal train pathway, Al-Qurayyat City in Saudi Arabia. *Environ. Sustain. Indic.* **2022**, *15*, 100184. [CrossRef]
38. Miller, C.A. Fifty years of EPA science for air quality management and control. *Env. Manag.* **2021**, *67*, 1017–1028. [CrossRef]
39. Pal, S.; Sharma, A. Satellite-Based Mapping for Seasonal Variations of Air Pollution and its Environmental Effects in Odisha. *J. Indian Soc. Remote Sens.* **2024**, *52*, 2039–2055. [CrossRef]
40. Box, G.; Jenkins, G.M. *Analysis: Forecasting and Control*; Holden Day: San Francisco, CA, USA, 1976.
41. Adam, M.G.; Tran, P.T.M.; Balasubramanian, R. Air quality changes in cities during the COVID-19 lockdown: A critical review. *Atmos. Res.* **2021**, *264*, 105823. [CrossRef] [PubMed]
42. Khadom, A.A.; Albawi, S.; Abboud, A.J.; Mahood, H.B.; Hassan, Q. Predicting air quality index and fine particulate matter levels in Bagdad city using advanced machine learning and deep learning techniques. *J. Atmos. Sol.-Terr. Phys.* **2024**, *262*, 106312. [CrossRef]
43. Gagan, M.; Uniyal, D.P.; Chadha, K.; Sunil, K.; Gaurav, P.; Avinash, K.; Anjali, N.; Pawan, K. Impact of Pandemic COVID19 on Air and Water Quality in India: A Systematic Review. *Int. J. Eng. Adv. Technol.* **2022**, *11*, 149–167. [CrossRef]
44. Hashim, B.M.; Al-Naseri, S.K.; Al Maliki, A.; Sa'adi, Z.; Malik, A.; Yaseen, Z.M. On the investigation of COVID-19 lockdown influence on air pollution concentration: Regional investigation over eighteen provinces in Iraq. *Environ. Sci. Pollut. Res.* **2021**, *28*, 50344–50362. [CrossRef]
45. Allan, R.P.; Arias, P.A.; Berger, S.; Canadell, J.G.; Cassou, C.; Chen, D.; Cherchi, A.; Connors, S.L.; Coppola, E.; Cruz, F.A.; et al. Summary for Policymakers. In *Climate Change 2021: The Physical Science Basis. Contribution of Working Group I to the Sixth Assessment Report of the Intergovernmental Panel on Climate Change*; Cambridge University Press: Cambridge, UK; New York, NY, USA, 2023; pp. 3–32.
46. World Health Organization. *The World Health Report 2005: Make Every Mother and Child Count*; World Health Organization: Geneva, Switzerland, 2005.
47. Moussa, Y.; Alwehab, A. Evaluation of Climate Change Indicators for Bagdad City Using Remote Sensing Technology. *Iraqi J. Sci.* **2023**, *64*, 4290–4301. [CrossRef]
48. Tie, X.; Long, X.; Li, G.; Zhao, S.; Cao, J.; Xu, J. Ozone enhancement due to the photodissociation of nitrous acid in eastern China. *Atmos. Chem. Phys.* **2019**, *19*, 11267–11278. [CrossRef]
49. Mahal, S.H.; Al-Lami, A.M.; Mashee, F.K. Assessment of the impact of urbanization growth on the climate of baghdad province using remote sensing techniques. *Iraqi J. Agric. Sci.* **2022**, *53*, 1021–1034. [CrossRef]
50. Gelaro, R.; McCarty, W.; Suárez, M.J.; Todling, R.; Molod, A.; Takacs, L.; Randles, C.A.; Darmenov, A.; Bosilovich, M.G.; Reichle, R.; et al. The Modern-Era Retrospective Analysis for Research and Applications, Version 2 (MERRA-2). *J. Clim.* **2017**, *30*, 5419–5454. [CrossRef]
51. Liu, J.; Sun, Y.; Ren, K.; Zhao, Y.; Deng, K.; Wang, L. A Spatial Downscaling Approach for WindSat Satellite Sea Surface Wind Based on Generative Adversarial Networks and Dual Learning Scheme. *Remote Sens.* **2022**, *14*, 769. [CrossRef]
52. Xu, K.; Tian, Q.; Yang, Y.; Yue, J.; Tang, S. How up-scaling of remote-sensing images affects land-cover classification by comparison with multiscale satellite images. *Int. J. Remote Sens.* **2019**, *40*, 2784–2810. [CrossRef]
53. Loyola, D.G.; García, S.G.; Lutz, R.; Argyrouli, A.; Romahn, F.; Spurr, R.J.D.; Pedergnana, M.; Doicu, A.; García, V.M.; Schüssler, O. The operational cloud retrieval algorithms from TROPOMI on board Sentinel-5 Precursor. *Atmos. Meas. Tech.* **2018**, *11*, 409–427. [CrossRef]
54. Acker, J.G.; Leptoukh, G. Online analysis enhances use of NASA earth science data. *Eos Trans. Am. Geophys. Union* **2007**, *88*, 14–17. [CrossRef]
55. Seinfeld, J.; Pandis, S. *Atmospheric Chemistry and Physics: From Air Pollution to Climate Change*, 3rd ed.; John Wiley & Sons: Hoboken, NJ, USA, 2016. Available online: https://books.google.nl/books?id=n_RmCgAAQBAJ (accessed on 16 August 2025).

56. Radmanesh, Y.; Tabrizi, M.S.; Etedali, H.R.; Azizian, A.; Babazadeh, H. Comparative evaluation of the accuracy of re-analysed and gauge-based climatic data in Iran. *J. Earth Syst. Sci.* **2023**, *132*, 190. [CrossRef]
57. Keys, R. Cubic convolution interpolation for digital image processing. *IEEE Trans. Acoust. Speech Signal Process.* **1981**, *29*, 1153–1160. [CrossRef]
58. Lehmann, T.M.; Gonner, C.; Spitzer, K. Survey: Interpolation methods in medical image processing. *IEEE Trans. Med. Imaging* **1999**, *18*, 1049–1075. [CrossRef] [PubMed]
59. Bisong, E. *Building Machine Learning and Deep Learning Models on Google Cloud Platform*, 1st ed.; OTTAWA: Apress Berkeley, CA, USA, 2019; p. XXIX–709. Available online: https://link.springer.com/book/10.1007/978-1-4842-4470-8 (accessed on 16 August 2025).
60. Paul, A.; Bhowmik, R.; Chowdary, V.M.; Dutta, D.; Sreedhar, U.; Ravi Sankar, H. Trend analysis of time series rainfall data using robust statistics. *J. Water Clim. Change* **2017**, *8*, 691–700. [CrossRef]
61. Harris, C.R.; Millman, K.J.; van der Walt, S.J.; Gommers, R.; Virtanen, P.; Cournapeau, D.; Wieser, E.; Taylor, J.; Berg, S.; Smith, N.J.; et al. Array programming with NumPy. *Nature* **2020**, *585*, 357–362. [CrossRef]
62. Hunter, J.D. Matplotlib: A 2D Graphics Environment. *Comput. Sci. Eng.* **2007**, *9*, 90–95. [CrossRef]
63. Yuan, D.F.; Liu, Y.; Trabelsi, T.; Zhang, Y.R.; Li, J.; Francisco, J.S.; Guo, H.; Wang, L.-S. Probing the dynamics and bottleneck of the key atmospheric SO2 oxidation reaction by the hydroxyl radical. *Proc. Natl. Acad. Sci. USA* **2024**, *121*, e2314819121. [CrossRef]
64. Sun, W.; Berasategui, M.; Pozzer, A.; Lelieveld, J.; Crowley, J.N. Kinetics of OH+SO_2+M: Temperature-dependent rate coefficients in the fall-off regime and the influence of water vapour. *Atmos. Meas. Tech.* **2022**, *22*, 4969–4984. [CrossRef]
65. Hoyle, C.R.; Fuchs, C.; Järvinen, E.; Saathoff, H.; Dias, A.; El Haddad, I.; Gysel, M.; Coburn, S.C.; Tröstl, J.; Bernhammer, A.-K.; et al. Aqueous phase oxidation of sulphur dioxide by ozone in cloud droplets. *Atmos. Chem. Phys.* **2016**, *16*, 1693–1712. [CrossRef]
66. Liu, T.; Chan, A.W.H.; Abbatt, J.P.D. Multiphase Oxidation of Sulfur Dioxide in Aerosol Particles: Implications for Sulfate Formation in Polluted Environments. *Environ Sci Technol.* **2021**, *55*, 4227–4242. [CrossRef]
67. Gao, J.; Wang, H.; Liu, W.; Xu, H.; Wei, Y.; Tian, X.; Feng, Y.; Song, S.; Shi, G. Hydrogen peroxide serves as pivotal fountainhead for aerosol aqueous sulfate formation from a global perspective. *Nat. Commun.* **2024**, *15*, 4625. [CrossRef] [PubMed]
68. Wang, J.; Li, J.; Ye, J.; Zhao, J.; Wu, Y.; Hu, J.; Liu, D.; Nie, D.; Shen, F.; Huang, X.; et al. Fast sulfate formation from oxidation of SO2 by NO2 and HONO observed in Beijing haze. *Nat. Commun.* **2020**, *11*, 2844. [CrossRef] [PubMed]
69. Liu, P.; Liu, Y.X.; Huang, Q.; Chao, X.; Zhong, M.; Yin, J.; Zhang, X.; Li, L.-F.; Kang, X.-Y.; Chen, Z.; et al. Sulfate formation through copper-catalyzed SO_2 oxidation by NO_2 at aerosol surfaces. *NPJ Clim. Atmos. Sci.* **2025**, *8*, 57. [CrossRef]
70. Ding, H.; Wang, H.; Huang, G.; Zhu, Y.; Zhang, L.; Zhang, X.; Zhou, M.; Wang, Q.; Li, X.; Xu, Q.; et al. Assessing the wastewater reclaim system consisted of wastewater plant-hybrid constructed wetland-ultra filtration and reverse osmosis in a chemical industrial park, a multi-criteria decision-making analysis. *Sci. Total Environ.* **2024**, *926*, 171942. [CrossRef]
71. Lv, X.; Lily, M.; Tasheh, S.N.; Ghogomu, J.N.; Du, L.; Tsona Tchinda, N. Enhanced Sulfate Formation from Gas-Phase SO_2 Oxidation in Non–•OH–Radical Environments. *Atmosphere* **2024**, *15*, 64. [CrossRef]
72. Pathak, M.; Patel, V.K.; Kuttippurath, J. Spatial heterogeneity in global atmospheric CO during the COVID-19 lockdown: Implications for global and regional air quality policies. *Environ. Pollut.* **2023**, *335*, 122269. [CrossRef]
73. Nisbet, E.G.; Manning, M.R.; Dlugokencky, E.J.; Fisher, R.E.; Lowry, D.; Michel, S.E.; Myhre, C.L.; Platt, S.M.; Allen, G.; Bousquet, P.; et al. Very Strong Atmospheric Methane Growth in the 4 Years 2014–2017: Implications for the Paris Agreement. *Glob. Biogeochem. Cycles* **2019**, *33*, 318–342. [CrossRef]
74. Abed, F.G. Spatiotemporal observations of CH_4 and CO_2 over Iraq using Atmospheric Infrared Sounder (AIRS) data. *J. Appl. Adv. Res.* **2020**, *5*, 6–10. [CrossRef]
75. de Vries, D.F.H.; Bernardo, C.H. Spatial and temporal variability in atmospheric CO_2 measurements. *Energy Procedia* **2011**, *4*, 5573–5578. [CrossRef]
76. Zhang, J.; Zhang, L.; Zhou, D.; Lv, H.; Cheng, C. Analysis of the temporal and spatial distribution of atmospheric CO_2 in China. *Mausam* **2018**, *69*, 459–464. Available online: http://103.215.208.102/index.php/MAUSAM/article/download/340/262 (accessed on 16 August 2025).
77. Abbas, N.M.; Rajab, J.M. Sulfur Dioxide (SO_2) anthropogenic emissions distributions over Iraq (2000–2009) using MERRA-2 data. *Al-Mustansiriyah J. Sci.* **2022**, *33*, 27–33. [CrossRef]
78. Szopa, S.; Naik, V.; Adhikary, B.; Artaxo, P.; Berntsen, T.; Collins, W.D.; Fuzzi, S.; Gallardo, L.; Kiendler-Scharr, A.; Klimont, Z.; et al. Chapter 6: Short-Lived Climate Forcers. In *Climate Change 2021: The Physical Science Basis Contribution of Working Group I to the Sixth Assessment Report of the Intergovernmental Panel on Climate Change*; Masson-Delmotte, V., Zhai, P., Pirani, A., Connors, S.L., Péan, C., Berger, S., Caud, N., Chen, Y., Goldfarb, L., Gomis, M.I., Eds.; Cambridge University Press: Cambridge, UK; New York, NY, USA, 2021; pp. 817–922. Available online: https://www.ipcc.ch/report/ar6/wg1/chapter/chapter-6/#6.3.2.1 (accessed on 15 February 2025).

79. Namdari, S.; Karimi, N.; Sorooshian, A.; Mohammadi, G.; Sehatkashani, S. Impacts of climate and synoptic fluctuations on dust storm activity over the Middle East. *Atmos. Environ.* **2018**, *173*, 265–276. [CrossRef] [PubMed]
80. Hossin, M.A.; Haque, A.; Saha, O.R.; Islam, R.; Shimin, T.I. A spatiotemporal analysis of air pollutants during and after COVID-19: A case study of Dhaka Division using Google Earth Engine. *DYSONA - Appl. Sci.* **2025**, *6*, 411–421. [CrossRef]

Disclaimer/Publisher's Note: The statements, opinions and data contained in all publications are solely those of the individual author(s) and contributor(s) and not of MDPI and/or the editor(s). MDPI and/or the editor(s) disclaim responsibility for any injury to people or property resulting from any ideas, methods, instructions or products referred to in the content.